UC San Diego

Title

Modal Analysis of Two-Dimensional Wakes With Different Cross-Sections

Permalink

Author

Luo, Chenyao

Publication Date

2023

UNIVERSITY OF CALIFORNIA SAN DIEGO

Modal Analysis of Two-Dimensional Wakes With Different Cross-Sections

A thesis submitted in partial satisfaction of the
requirements for the degree Master of Science

in

Engineering Science (Mechanical Engineering)

by

Chenyao Luo

Committee in charge:

Professor Sutanu Sarkar, Chair
Professor Xuanting Hao
Professor Oliver T. Schmidt

2023

The Thesis of Chenyao Luo is approved, and it is acceptable in quality and form for publication on microfilm and electronically.

University of California San Diego

2023

TABLE OF CONTENTS

LIST OF FIGURES

LIST OF TABLES

ACKNOWLEDGEMENTS

I would like to acknowledge Professor Sarkar for his support as the chair of my committee. I also want to thank Professor Schmidt and Professor Hao for being on my committee. I would like to thank all from the Lab who gave guidance to my research and thesis. I also want to thank my family and friends for their love and support.

ABSTRACT OF THE THESIS

Modal Analysis of Two-Dimensional Wakes With Different Cross-Sections

by

Chenyao Luo

Master of Science in Engineering Science (Mechanical Engineering)

University of California San Diego, 2023

Professor Sutanu Sarkar, Chair

Two-dimensional flow over a cylinder is simulated using Ansys Fluent and analyzed using spectral proper orthogonal decomposition (SPOD). Wakes past bluff bodies are common in nature and the understanding of these wakes is crucial to mechanical and environmental engineering. Two-dimensional wakes serve as a good model for the dominant large-scale dynamics of these types of wakes. The vortex shedding Strouhal numbers (St) and associated eigenmodes are extracted. We consider both the effect of the Reynolds number (Re) and the shape of the object by conducting a series of simulations. The effect of the Reynolds number is investigated by simulating circular cylinder wakes at Reynolds numbers at 60, 100, and 150. The influence of varying the shape of the bluff body is examined by conducting simulations

at Re = 150 for circular and square cylinders as well as elliptical cylinders with aspect ratios of 0.25, 0.5, and 4. As revealed by SPOD dominant frequencies, the VS Strouhal numbers vary as Reynolds number or body shape changes in a way that is consistent and in quantitative agreement with results from the literature. The spatial modes at *St* represent wave-like packets of perturbation traveling downstream, corresponding to the vortex-shedding motions. The modes associated with harmonics of the base frequency (*St*, 2*St*, 3*St*, ...) alternate between symmetric and antisymmetric shapes for all cases examined. As the aspect ratio changes from 0.25 to 4, the wakes evolve from bluff body wakes towards slender body wakes, featuring Karman vortices with higher spacing. Particularly, in the case with AR = 0.25, a secondary vortex street emerges in the far wake, characterized by a much larger physical scale and lower frequency as compared to the primary Karman wake.

Chapter 1

Introduction

Flow past cylinder has always been a classical problem in theoretical and computational fluid dynamics. The vortex shedding in the wake behind a cylinder of circular cross-section has been studied by many. Barkley (2006), Kumar and Mittal (2006), Mittal (2008), and Roshko (1953) analyzed two-dimensional flow over the circular cylinder with low Reynolds numbers (*Re*) numerically and performed linear stability analysis of the flow. Barkley and Henderson (1996), Leontini, Thompson, and Hourigan (2010), and Ma and Karniadakis (2002) numerically analyzed the transition of two-dimensional wake to three-dimensional unsteadiness. Other than numerical simulations, experiments were done to investigate two-dimensional flow over cylinders. Gharib and Derango (1989) and Wen and Lin (2001) used soap films, Tritton (1959) used quartz fibers to conduct the experiments. Most of the simulations conducted linear stability analysis on the flow to find the non-dimensional vortex shedding frequency, the Strouhal number (*St*), and the eigenmodes of the flow. Williamson and Brown (1998) and Fey, König, and Eckelmann (1998) gathered experimental *St* data from literature and calculate correlation equations between *Re* and *St*.

Other than the circular cylinder, cylinders of different shapes have also been studied. Robichaux, Balachandar, and Vanka (1999), Franke, Rodi, and Schönung (1990), Kelkar and Patankar (1992), and Sohankar, Norberg, and Davidson (1998) did numerical simulation of two-dimensional flow over square cylinders and calculated the *St*. Davis, Moore, and Purtell (1984)

compared the numerical data to experimental data obtained by taking smoke-wire photographs from a wind tunnel test. Besides square cylinders, flow over elliptical cylinders with different aspect ratios is a topic of interest. Thompson, Radi, Rao, Sheridan, et al. (2014) and Shi, Alam, and Bai (2020) simulated two-dimensional flow over elliptical cylinders, from circular cylinder to flat plate, numerically. The Strouhal number behavior for different shapes and different Reynolds numbers seems different and is a topic of interest. The objective of the present thesis research is to analyze the flow over cylinders with different shapes at different Reynolds numbers while remaining in the unsteady, 2D regime.

Ansys Fluent is a commercial software that allows users to build cases from scratch and simulate the flow numerically. In this study, we will use Ansys Fluent for flow simulations. A free academic version available to university students is used here. Spectral proper orthogonal decomposition (SPOD), a modal analysis method, proposed by Picard and Delville (2000), can be used to analyze flow data. SPOD is a method that can extract eigenvalues and eigenvectors (energy modes) from flow data. Analyzing flow data using SPOD, we can calculate the Strouhal number and energy modes. SPOD is a less commonly used method than temporal power spectra and we want to see how well the SPOD method performs in analyzing the two-dimensional flow. After the simulation is done in Ansys Fluent, SPOD modal analysis will be performed on the flow data. The resulting Strouhal numbers and energy modes will be compared with results from the literature. In this paper, we will analyze three different Reynolds numbers of 60, 100, and 150, and three different shapes of circular, square, and elliptical cylinders with different values of aspect ratio.

Chapter 2

Methodology

2.1 Physical Modeling

The flow past a cylinder is simulated by solving 2D incompressible Navier-Stokes equations. The conservation equations of mass and momentum are solved:

$$\nabla \cdot \mathbf{u} = 0, \tag{2.1}$$

$$\frac{\partial \mathbf{u}}{\partial t} + \mathbf{u} \cdot \nabla \mathbf{u} = -\frac{1}{\rho} \nabla p + \frac{1}{Re} \nabla^2 \mathbf{u}, 0 \tag{2.2}$$

where $\mathbf{u} = (u, v)$ is the 2D velocity vector, ρ is the fluid density, Re is the Reynolds number. The boundaries are defined as inlet, outlet, cylinder wall, and top-bottom-wall boundaries. The boundary condition on cylinder wall is no-slip, $\mathbf{u} = (0,0)$. The inlet has a Dirichlet boundary condition with $\mathbf{u} = (U_\infty, 0)$ and $p = p_\infty$, where U_∞ is freestream velocity p_∞ is the ambient pressure. The outlet is also a Dirichlet boundary with $p = p_\infty$. The top and bottom walls are set as far-field with $\mathbf{u} = (U_\infty, 0)$ and $p = p_\infty$. For the 2D simulation, the direction parallel to the free-stream flow is defined as the x-axis, and the direction normal to the free-stream flow is defined as the y-axis. The cylinder is centered at the origin (0,0).

2.2 Numerical Scheme

The simulation is done in Ansys Fluent. Fluent uses the finite volume method (FVM) to solve the governing equations. The finite volume method interprets grid cells as control volumes in the integral form of partial differential equations and evaluates the average value of the solution over the control volumes. The Fluent option of pressure-based solver, absolute velocity formulation, transient time, and 2D planar space is used. The laminar model is selected for the viscous terms. The SIMPLE (Semi-Implicit Method for Pressure Linked Equations) scheme is chosen for pressure-velocity coupling. SIMPLE algorithm is an iterative pressure correction method that solves the discretized momentum equation and pressure correction equation implicitly and the velocity correction equation explicitly. The algorithm first solves the discretized momentum equation

$$A\mathbf{u} - \frac{\mathbf{u}_0}{\Delta t} = -\nabla p,$$

$$a_p \mathbf{u}_p + \sum_n a_{n,p} \mathbf{u}_{n,p} - \frac{\mathbf{u}_0}{\Delta t} = -\nabla p \tag{2.3}$$

for $\mathbf{u}$ where $\nabla \cdot \mathbf{u} \neq 0$, where $\mathbf{u}_0$ is the initial guess of velocity, a_p is the diagonal part of matrix A, $a_{n,p}$ is the off-diagonal part of matrix A, $\mathbf{u}_{n,p}$ is the velocity at n^{th} time step, and n is the time step. Next, we solve the pressure correction equation

$$\nabla \cdot [(a_p^{-1})_f \nabla p] = \nabla \cdot [a_p^{-1} (\frac{\mathbf{u}_0}{\Delta t} - \sum_n a_{n,p} \mathbf{u}_{n,p})]_f \tag{2.4}$$

for p, where f subscript means in terms of flux. Then we use

$$\mathbf{u}_f \cdot \mathbf{S}_f = [a_p^{-1} (\frac{\mathbf{u}_0}{\Delta t} - \sum_n a_{n,p} \mathbf{u}_{n,p})]_f \cdot \mathbf{S}_f - (a_p^{-1})_f \nabla_f p \cdot \mathbf{S}_f, \tag{2.5}$$

where $\mathbf{u}_f$ is face velocity and $\mathbf{S}_f$ is surface vector, to correct $\mathbf{u}$ such that $\nabla \cdot \mathbf{u} = 0$ but $A\mathbf{u} \neq -\nabla P + \frac{\mathbf{u}_0}{\Delta t}$. Iterate equations 2.3 through 2.5 until the Navier-Stokes equations are satisfied.

For spatial discretization, the least-squares cell-based method is selected for gradient, second-order method for pressure, and second-order upwind method for momentum. The least-squares cell-based method calculates the gradient in a cell by minimizing error in least-squares sense to extrapolate the cell value to the centers of all neighboring cells. The gradient is calculated by summing the multiplication of the weight factor and the difference vector between the cell center and the neighboring cell center for all neighboring cells. The second-order scheme interpolates the pressure values at the faces using the momentum equation for second-order accurate convection terms. Upwind scheme uses data points biased to be more "upwind" to calculate the derivatives in a flow field. The second-order upwind scheme is second-order accurate and is defined as

$$u_x^- = \frac{3u_i^n - 4u_{i-1}^n + u_{i-2}^n}{2\Delta x}, \tag{2.6}$$

$$u_x^+ = \frac{-u_{i+2}^n + 4u_{i+1}^n - 3u_i^n}{2\Delta x}. \tag{2.7}$$

For transient formulation, the second-order implicit method is used. Standard initialization is chosen with fixed time steps. The cylinder wall is set to no-slip boundary condition. The top-bottom-walls boundaries are set as free-slip walls with zero shear. Velocity inlet condition is used with an initial x-velocity of 1 m/s. Pressure outlet condition is used with gauge pressure of 0 Pa, pressure profile multiplier of 1, and no backflow. The rest of the setting remains unchanged. For the fluid, we defined the physical properties. The free-stream velocity (U_∞) is set to 1 m/s, density (ρ) to 1 kg/m^3, and characteristic length (L) as the diameter of cylinder normal to the flow (D) to 1 m. Most parameters are kept the same for all simulation cases. The dynamic viscosity (μ) will be manipulated to achieve the desired Reynolds number. This method is equivalent to solving the nondimensional NS equations with free-stream velocity, free-stream density, and cylinder diameter as the reference scales for velocity, density, and length. The time step is set to 0.1 seconds and the maximum iterations of the SIMPLE algorithm per time step is 25. The total time steps are 3000 which grants 300 D/U_∞ of time interval.

2.3 Domain and Grid

The computational domain is L_x by L_y, where L_x is the x-direction domain length and L_y is the y-direction domain length. The computational domain is set to $30D$ in the x-axis and $20D$ in the y-axis. The cylinder is centered at (0,0) with $10D$ upstream, $20D$ downstream, and $10D$ above and below the centerline y = 0. The grid generated by Ansys Fluent is unstructured.
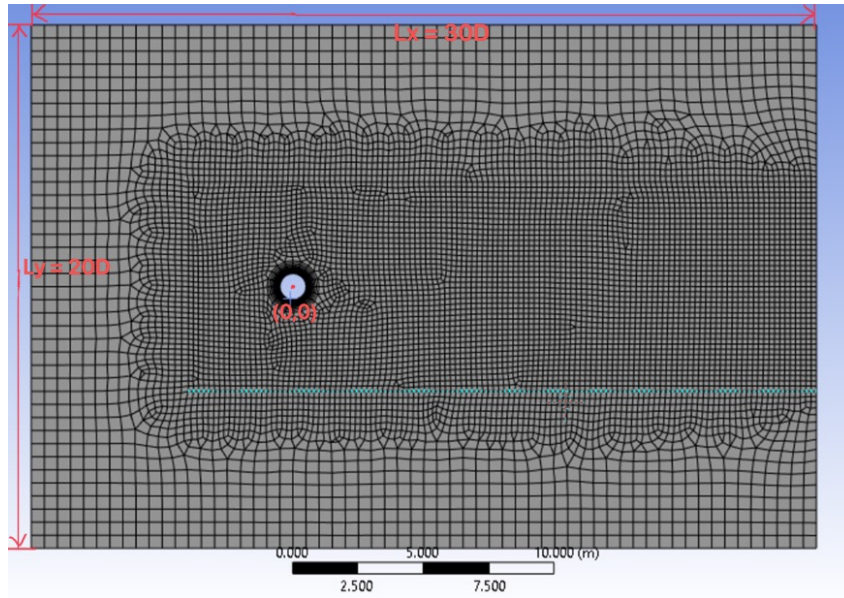
Figure 2.1. Unstructured body-fitted grids generated with Ansys Fluent. The streamwise and transverse extents of the domain are defined as L_x and L_y and the cylinder is placed at the origin. The grid is denser near the body to capture the attached laminar boundary layer, separation, and the near-wake structures.

2.3.1 Grid Independence Study

The power spectral density (P) describes the spectral power distribution per unit time. Power spectral density is calculated using the Fast Fourier Transform (FFT). FFT is a discrete Fourier transform that converts a signal from its original domain to the frequency domain. The frequency at which the power spectral density is concentrated is the dominant frequency, which for a cylinder, is the vortex shedding frequency.

Two grid choices are tested for grid independence. For the first grid choice (Grid 1), the

maximum element sizes are set as $0.1D$ near the centerline and $0.5D$ far-field. The second grid choice (Grid 2) sets the maximum element size to $0.05D$ near the centerline and $0.1D$ far-field. The case of $Re = 100$ is tested for the two grid choices. The one-point spectrum is plotted for comparison in Figure 2.2. The frequency peaks are at 0.15 for both cases. The mean lift coefficients are 0.0017 and 0.0020 and the mean drag coefficients are 1.3983 and 1.4019. The differences are negligible and Grid 1 is chosen for our study.

(a) Grid 1   **(b)** Grid 2
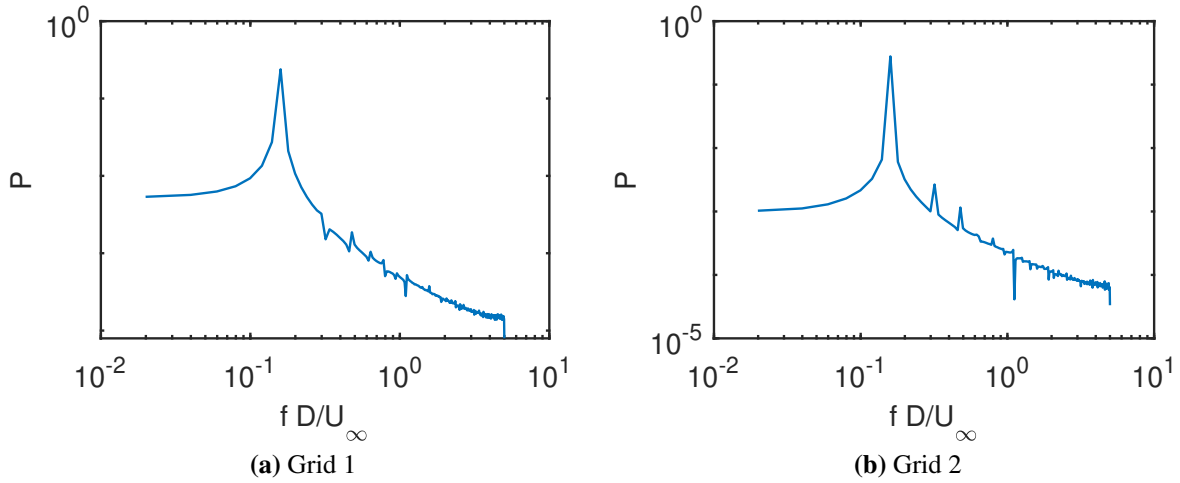
Figure 2.2. One point spectrum, in case Re=100, cylinder wake, using Grid 1 and Grid 2. The peak frequencies are both at 0.1596, indistinguishable at the present frequency resolution.

2.4 Spectral Proper Orthogonal Decomposition (SPOD)

Modal analysis will be performed on the flow data after simulation. In this section, we will introduce the method: spectral proper orthogonal decomposition (SPOD). SPOD is a modal decomposition method and is a spectral version of POD. SPOD method assumes statistically stationary time series. It finds the optimal orthogonal basis for the data that best represents the energy. SPOD modes are eigenvectors of the cross-spectral density tensors at each frequency. SPOD approximates a zero-mean stochastic process $\{\mathbf{q}(\mathbf{x},\mathbf{t})\}$ by finding the deterministic function $\phi(\mathbf{x},t)$ from finite samples, where $\mathbf{x},t$ represents the spatial and temporal

variables. It is assumed that the process is defined in a Hilbert space with an inner product

$$\langle \mathbf{q}_1, \mathbf{q}_2 \rangle = \int_{-\infty}^{\infty} \int_{\Omega} \mathbf{q}_1^*(\mathbf{x}, t) \mathbf{W}(\mathbf{x}) \mathbf{q}_2(\mathbf{x}, t) \, \mathrm{d}\mathbf{x} \, \mathrm{d}t. \tag{2.8}$$

The SPOD problem maximizes the projection of the signal on the basis:

$$\lambda = \frac{E\{|\langle \mathbf{q}(\mathbf{x}, t), \phi(\mathbf{z}) \rangle|^2\}}{\langle \phi(\mathbf{z}), \phi(\mathbf{z}) \rangle}, \tag{2.9}$$

where $E\{\cdot\}$ is the expectation operator over the probability space. The resulting eigenvalue problem is

$$\int_{-\infty}^{\infty} \int_{\Omega} \mathbf{C}(\mathbf{x}, \mathbf{x}', t, t') \mathbf{W}(\mathbf{x}') \phi(\mathbf{x}', t') \, \mathrm{d}\mathbf{x}' \, \mathrm{d}t' = \lambda \phi(\mathbf{x}, t), \tag{2.10}$$

where

$$\mathbf{C}(\mathbf{x}, \mathbf{x}', t, t') = E\{\mathbf{q}(\mathbf{x}, t) \mathbf{q}^*(\mathbf{x}', t')\} = \mathbf{C}(\mathbf{x}, \mathbf{x}', \tau) \tag{2.11}$$

is the two-point, two-time covariance tensor where $\tau = t - t'$ assuming time homogeneity. SPOD is analyzed in the frequency domain. Fourier transform on the correlation tensor gives the cross-spectral density tensor $\mathbf{S}$:

$$\mathbf{S}(\mathbf{x}, \mathbf{x}', f) = \int_{-\infty}^{\infty} \mathbf{C}(\mathbf{x}, \mathbf{x}', \tau) e^{i2\pi f \tau} \, \mathrm{d}\tau. \tag{2.12}$$

The spectral eigenvalue problem is then

$$\int_{\Omega} \mathbf{S}(\mathbf{x}, \mathbf{x}', f') \mathbf{W}(\mathbf{x}') \psi(\mathbf{x}', f') \, \mathrm{d}\mathbf{x}' = \lambda(f') \psi(\mathbf{x}, f'). \tag{2.13}$$

$\phi(\mathbf{x}, t) = \psi(\mathbf{x}', f') e^{i2\pi f' t}$ is an eigenvector of the eigenvalue problem. For the discrete form of SPOD, we arrange simulation data into a matrix

8

$$Q = \begin{bmatrix} | & | & & | \\ \mathbf{q}^{(1)} & \mathbf{q}^{(2)} & \cdots & \mathbf{q}^{(N)} \\ | & | & & | \end{bmatrix}, \quad Q \in \mathbb{C}^{M \times N_t} \tag{2.14}$$

where N_t is the total number of snapshots, M is the degree of freedom, and $\mathbf{q}^{(k)}$ is the kth snapshot of data. The covariance tensor is estimated as

$$C = \frac{1}{N_t - 1} QQ^H, \tag{2.15}$$

where $(\cdot)^H$ is the Hermitian transpose. The eigenvalue problem becomes

$$CW\Phi = \Phi\Lambda \tag{2.16}$$

or using the method of snapshots[25]

$$Q^H W Q\Psi = \Psi\Lambda \qquad \Phi = Q\Psi \tag{2.17}$$

where eigenvectors and eigenvalues are

$$\Phi = \begin{bmatrix} | & | & & | \\ \Phi^{(1)} & \Phi^{(2)} & \cdots & \Phi^{(N)} \\ | & | & & | \end{bmatrix}, \quad \Phi \in \mathbb{C}^{M \times N_t} \tag{2.18}$$

and

$$\Lambda = \begin{bmatrix} \lambda_1 & & & \\ & \lambda_2 & & \\ & & \ddots & \\ & & & \lambda_N \end{bmatrix}. \tag{2.19}$$

9

λ_k, $\Phi^{(k)}$, $\Psi^{(k)}$ are the singular values, left singular vectors, and right singular vectors of the data matrix. The SPOD modes are eigenvectors of the CSD matrix at each frequency. For the N_t snapshots, we break them into N_{blk} blocks. For each block, N_{FFT} of snapshots are used for Fourier transform with N_{ovlp} overlapping snapshots between each block. The number of total blocks is

$$N_{blk} = \left\lfloor \frac{N_t - N_{ovlp}}{N_{FFT} - N_{ovlp}} \right\rfloor. \tag{2.20}$$

A more detailed explanation can be found in Schmidt and Colonius (2020) and Towne, Schmidt, and Colonius (2018).

In this study, vorticity is of primary interest, and SPOD analysis is done on vorticity. We will use $N_t = 1,500$ data snapshots after reaching the statistically stationary state. The $N_{FFT}=256$ and $N_{ovlp}=128$. The weight matrix is $\mathbf{W}(x,y) = \left[\frac{\Delta x \Delta y}{\Sigma_{\Omega}(\Delta x \Delta y)} \right]$, which is the weights of numerical quadrature over the entire domain. By performing SPOD, we expect to get the frequency spectra, the dominant Strouhal numbers, and the energetic modes of the flow.

Chapter 3

Circular Cylinder Flow

3.1 Parameters

The circular cylinder flows are simulated at three different Reynolds numbers $Re = DU_\infty/\nu$: 60, 100, and 150, where D is the object diameter perpendicular to the freestream, U_∞ is the freestream velocity, and ν is the kinematic viscosity. As a result, the coefficient of the viscous term in the non-dimensional governing equations 2.1-2.2 is $1/Re$.

For SPOD analysis, we interpolate the unstructured grid into a structured Cartesian grid. Quadrilateral grids are used with finer grids near the cylinder and coarser near boundaries. The interpolated grid size between $\pm 4D$ in the y-axis and $-4D$ and $20D$ in the x-axis is $0.1D$. The rest of the domain has a grid size of $0.5D$.

3.2 Validation

3.2.1 Flow Visualization

After the simulation is done in Ansys Fluent, we export flow data, including velocity, lift, drag, vorticity, etc. for further analysis. The flow is visualized in MATLAB by plotting instantaneous vorticity. The vorticity plots shown in Figure 3.1 are obtained after the statistically stationary state is reached. The vortices formed behind the body alternates periodically at the vortex shedding frequency. The vortices for circular cylinders have the pattern of Karman vortex street, while the downstream separation distance between vortices is reduced as the Reynolds

number is increased. In all three cases, the Karman vortex street is unsteady but laminar. The figures show that the vortices are tightly packed and the shedding frequency is higher at a higher Reynolds number, as will be quantified later.
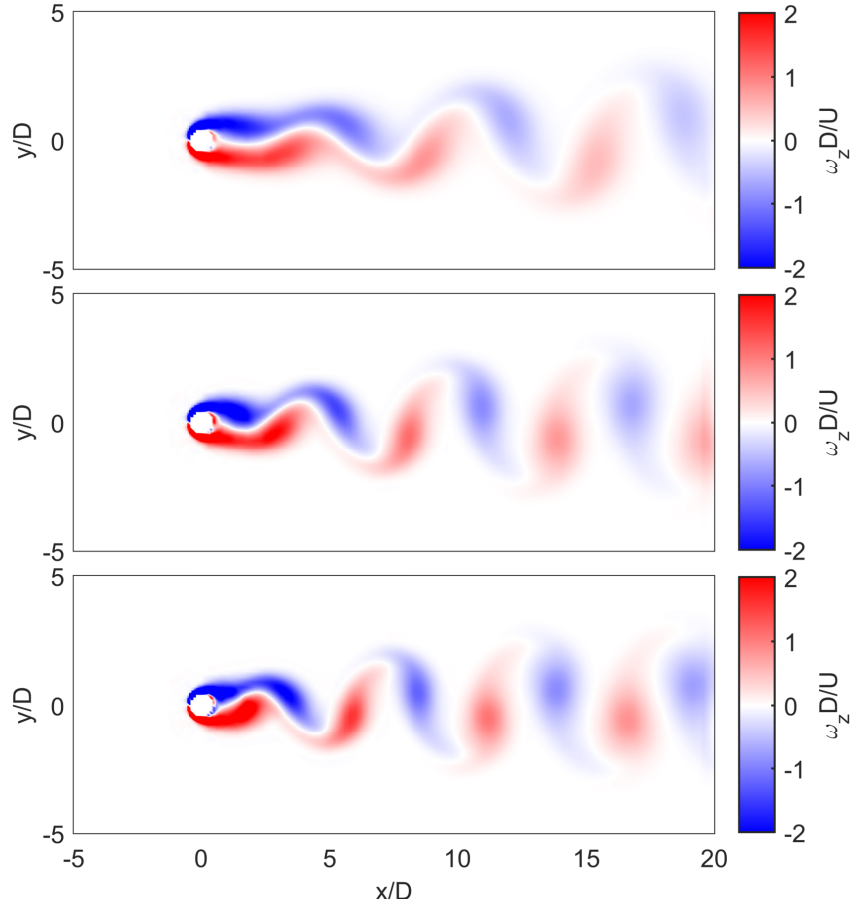
Figure 3.1. Visualization of vorticity plots normalized by convective units (*U* and *D*) at Reynolds numbers of 60(top), 100(middle), and 150(bottom). It can be seen that the length of the attached shear layer decreases with Reynolds number, and the separation of vortices also decreases with Reynolds number.

3.2.2   Lift and Drag

Lift coefficient (C_l) and Drag coefficient (C_d) are the non-dimensionalized lift and drag properties. For 2D flow, they are defined as

$$C_D = \frac{2F_d}{\rho U_\infty^2 D} \quad and \quad C_L = \frac{2F_l}{\rho U_\infty^2 L} \quad , \tag{3.1}$$

12
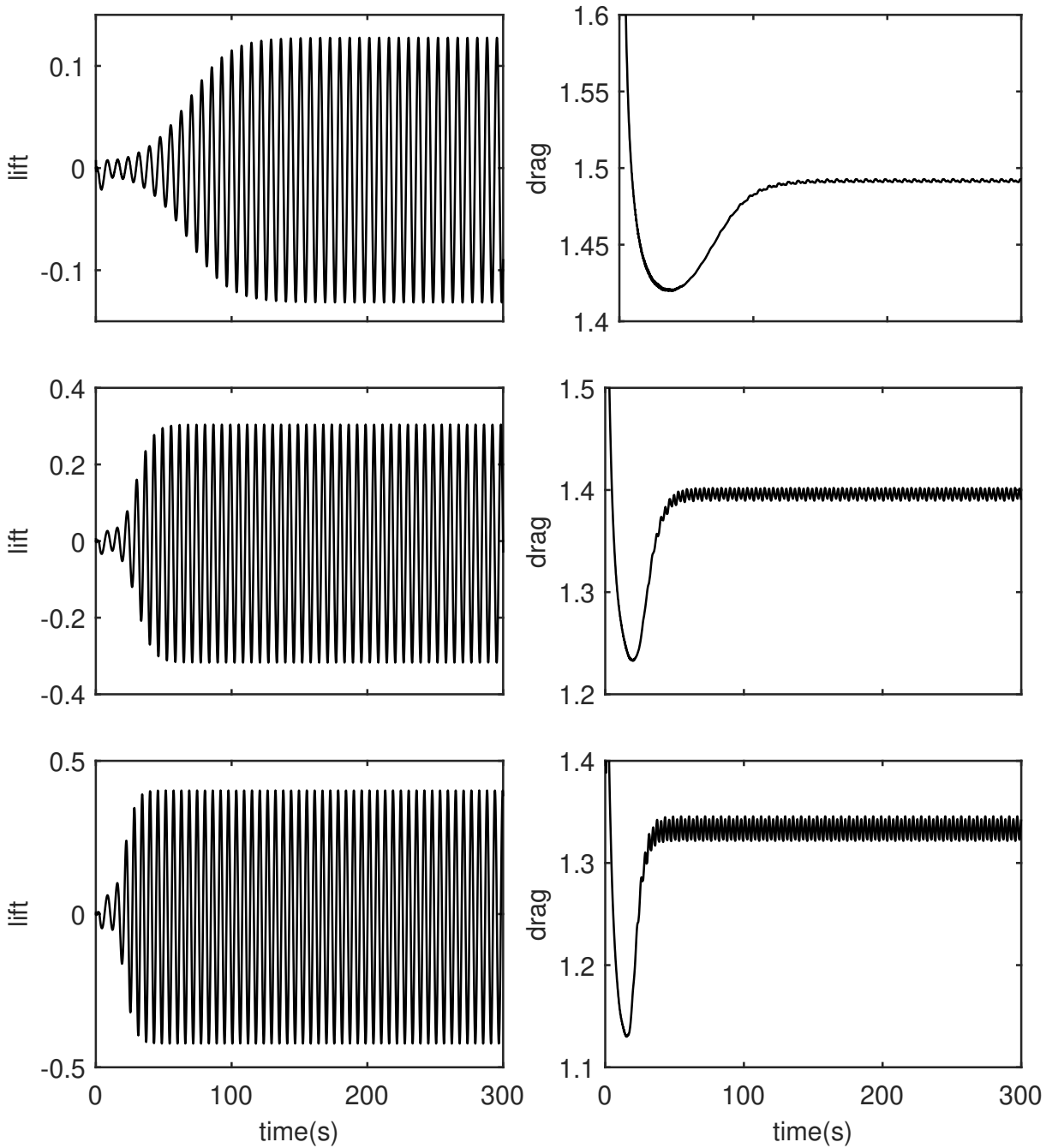
Figure 3.2. Evolution of lift and drag coefficients in time for flow over a circular cylinder at *Re* of 60(top), 100(middle), and 150(bottom). The lift and drag coefficients in Table 3.1 are calculated as the time average of the instantaneous lift and drag coefficients in the statistically stationary stage.

Table 3.1. Mean drag coefficients for circular cylinder flow.

Re	Present C_d	Experimental C_d	Relative Difference(%)	Numerical C_d	Relative Difference(%)
60	1.4853	1.5330[22]	3.11	1.47[29]	1.04
100	1.3958	1.4351[22]	2.74	1.3512[16]	3.30
150	1.3329	1.3910[22]	4.18	1.334[16]	0.08

where F_d is the time-averaged drag force and F_l is the time-averaged lift force exported from Ansys Fluent. The lift and drag coefficients are plotted as a function of the time step shown in Figure 3.2. From Figure 3.2, we can see that after 150s all cases reach the stationary state. Thus the last 1500 snapshots, from $\frac{tU_\infty}{D} = 150$ to $\frac{tU_\infty}{D} = 300$ will be used for SPOD analysis. The time to reach the statistically stationary state is shorter when *Re* is higher as seen in Figure 3.2. The mean drag coefficients are calculated by averaging the data sets after reaching the statistically stationary state. The drag coefficients are shown in Table 3.1. The drag coefficient is lower at a higher Reynolds number. The reason for the decrease of drag coefficient can be due to the change of flow separation point.

Table 3.1 also compares the results obtained from Fluent with experimental calculations of Schlichting and Gersten(2017) and numerical calculations from Tritton(1959) and Liu, Zheng, Liao, Sung, et al.(1998). Both experimental and numerical results from the literature express the same trend as our results. The experimental drag coefficients are higher than the numerical ones in general. The results from the present study, calculated from numerical simulation, are closer to previous numerical results. The accuracy of results compared to the numerical calculations has an average of 1.47% difference. The overall mean difference of Fluent simulated drag coefficients compared to the literature is 2.41%. The difference is small.

(a) Re=60   **(b)** Re=100   **(c)** Re=150
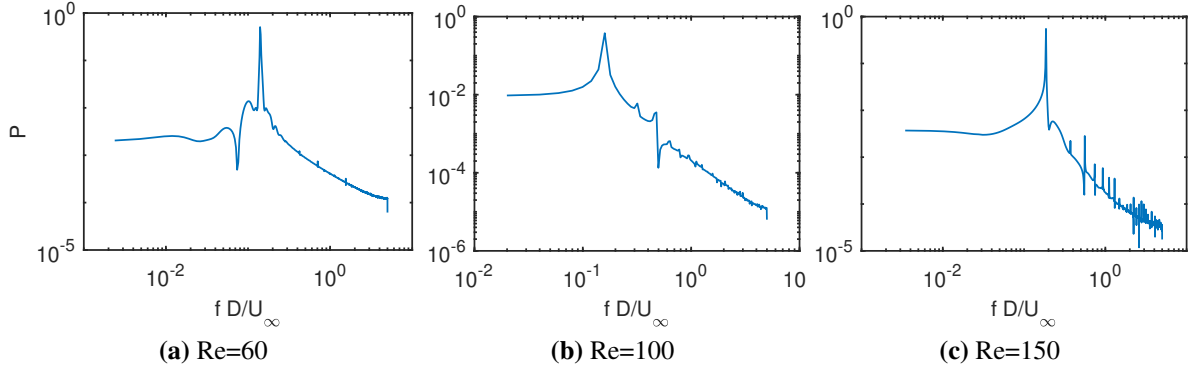
Figure 3.3. One point power spectrum for *Re* of 60 (a), 100 (b), 150 (c) with non-dimensional peak frequencies(Strouhal numbers) at 0.1404, 0.1594, and 0.1861. This dominant frequency is the vortex shedding frequency.

3.2.3 One-Point Spectrum

The most prominent feature of the Karman wake is periodic vortex shedding, which is characterized by a principle frequency $-f$. To quantify it, we perform the discretized Fourier transform on the time series of ω_z. The vorticity data at a selective point downstream are exported for each case. Fast Fourier Transform is done on the vorticity data and the results are plotted as power spectral density shown in Figures 3.3. The Strouhal numbers, non-dimensional shedding frequency $St = fD/U_\infty$, are the peak PSD frequencies of 0.1404, 0.1594, and 0.1861. The Strouhal number is larger at higher *Re*. An empirical relation between *Re* and *St* in the *Re* range suitable for this work is proposed by Williamson and Brown(1998),

$$St = 0.2665 - \frac{1.018}{\sqrt{Re}}. \tag{3.2}$$

The calculated *St* at the three *Re* are 0.1351, 0.1647, and 0.1834. There is about a 2.87% average difference between the results.

15

3.3   SPOD Analysis

After simulation in Fluent, we export the flow property data and use Fortran to perform the SPOD on vorticity data. Eigenspectra and eigenvectors are calculated and used to present the enstrophy distribution among frequencies and the spatial modes associated with the dominant frequencies.

3.3.1   SPOD Spectra

(a) Re=60   **(b)** Re=100   **(c)** Re=150
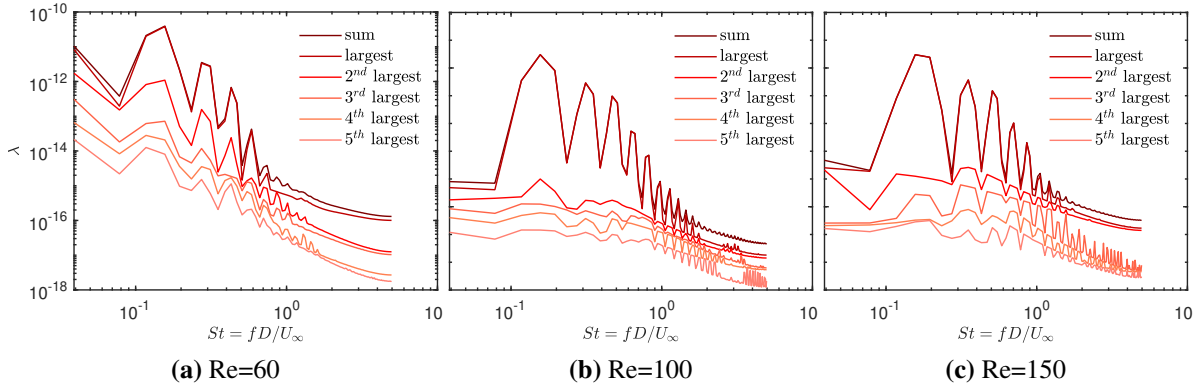
Figure 3.4. SPOD spectra for circular cylinder flow at Re = 60(left), 100(middle), 150(right). The non-dimensional vortex shedding Strouhal numbers are 0.1367, 0.1614, and 0.1823.

The SPOD eigenvalues are plotted with respect to the Strouhal number in Figure 3.4. The darkest line represents the sum of all eigenvalues and the rest represents the rank of eigenvalues from largest to 5th largest with colors of decreasing intensity. The gap between the largest and second largest eigenvalue is the greatest among all indicating a very strong low-rank behavior. The difference between the leading mode and the rest increases as Re increases within the examined range of Re. The spectrum of leading SPOD modes has the first peaks at St = 0.1367, 0.1614, and 0.1823, which is also shown in Table 3.2. The $St - Re$ relationship obtained from one-point spectra and SPOD analysis both agree well with the experimental correlation, (3.2). Numerical and experimental data from the literature are also presented in Table 3.2. The relative difference between the literature data and data from the present study is shown in the Table

16

as well. The overall percent error is around 3.47% on average. A comparison of St from the one-point spectrum, SPOD analysis, and Williamson's[32] is shown in Figure 3.5. The SPOD St aligns closer to the curve than St from the one-point spectrum. We conclude that the results from this study are comparable to the data from the literature.
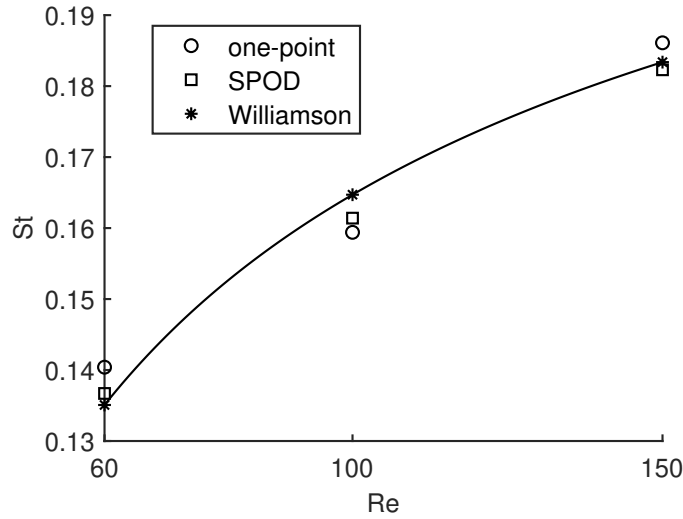
Figure 3.5. The resulting St from one-point spectrum, SPOD spectrum, and Williamson[32] at $Re = 60, 100, 150$. The curve is plotted using equation 3.2 from Williamson.

3.3.2   SPOD Modes

The modes associated with St, $2St$, and $3St$ are plotted. The leading energy modes, associated with the largest eigenvalue at frequencies of St, $2St$, and $3St$, are shown in Figure 3.6. The leading modes associated with St and $3St$ are symmetric to the centerline. The leading mode associated with $2St$ is anti-symmetric to the centerline. The most energetic mode is the symmetric perturbation at St resulting in symmetric St modes. This mode has a standing-wave-like feature which means it has constant advection velocity. The mean wake is anti-symmetric. The reason that there is a change from anti-symmetry to symmetry of the St mode is that symmetry is broken during the first Hopf bifurcation from steady to periodic shedding. The symmetric perturbation acts on anti-symmetric base flow causing the symmetry-breaking bifurcation. The leading mode associated with $2St$ is anti-symmetric about centerline and interchanges between positive and

17

Table 3.2. Strouhal numbers of Circular Cylinder Flow

Source	Re	St	Relative Difference(%)	Method
This study	60	0.1367	—-	Numerical
Williamson[32]		0.1351	1.18	Numerical
Barkley[2]		0.135	1.26	Numerical
Roshko[21]		0.13	5.15	Experimental
Gharib[10]		0.132	3.56	Experimental
Wen[31]		0.14	2.36	Experimental
This study	100	0.1614	—-	Numerical
Williamson[32]		0.1647	2	Numerical
Barkley[2]		0.171	5.61	Numerical
Braza[4]		0.16	0.88	Numerical
Roshko[21]		0.17	5.06	Experimental
Gharib[10]		0.173	6.7	Experimental
Wen[31]		0.175	7.77	Experimental
Berger[3]		0.15	7.6	Experimental
Tritton[29]		0.16	0.88	Experimental
Freihe[9]		0.16	0.88	Experimental
This study	150	0.1823	—-	Numerical
Williamson[32]		0.1834	0.6	Numerical
Barkley[2]		0.18	1.28	Numerical
Roshko[21]		0.174	4.77	Experimental
Wen[31]		0.176	3.58	Experimental
Thompson[27]		0.184	4.46	Experimental

negative longitudinally.

(a) Re=60   **(b)** Re=100   **(c)** Re=150
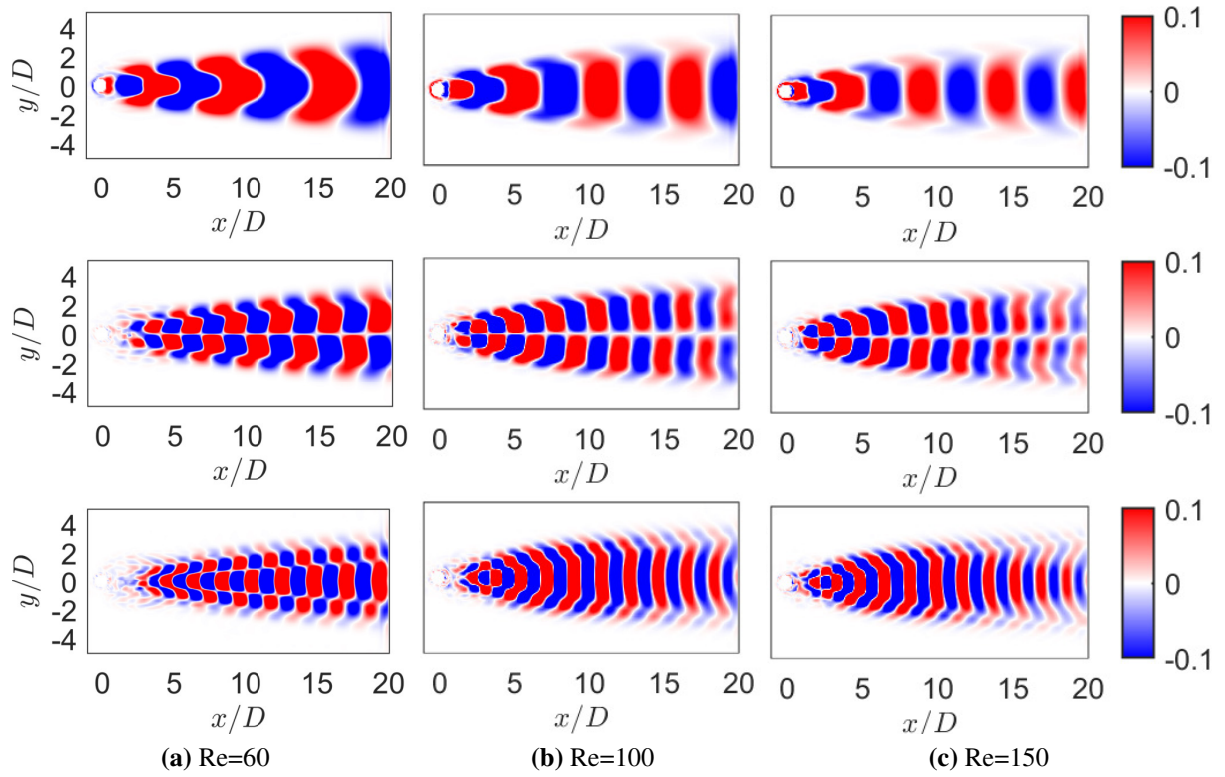
Figure 3.6. The leading SPOD modes at *St*(top), 2*St*(middle), and 3*St*(bottom) at *Re* = 60(left), 100(middle), and 150(right). Since the SPOD modes are eigenvectors, they are free up to a scalar multiple. To show the relative amplitude difference, the modes are normalized by the largest amplitude in the same plane.

Chapter 4

Effect of Body Shapes on the Flow

The wake generated behind a body depends largely on the shape, ranging from bluff body wake such as the wake of a flat plate to slender body wake such as the wake of a high aspect ratio prolate body. In this work, we will experiment on the shape of the wake generator by changing the aspect ratio of an elliptical cylinder and comparing those wakes with the wake of a circular and a square cylinder. The same methods as in Chapter 3 will be used for simulation and SPOD analysis. The unstructured body-fitted grid will be adjusted according to the shape of the cylinder but the interpolated grid will be the same as previous. In this chapter, we will discuss two specific shapes: square and elliptical cylinders.

4.1 Comparison of a Square Cylinder to a Circular Cylinder

In this section, we will show simulation results for flow over a square cylinder at Re of 60, 100, and 150. The flow properties and SPOD analysis results will be compared to the literature and also to the data from circular cylinder flow.

4.1.1 Flow Visualization

The flow is visualized in Figure 4.1. The flow has Karman vortex street features for all Reynolds numbers. Similar to circular cylinder flow, the vortex shedding is faster at a higher Reynolds number. The lift and drag coefficients are plotted with respect to time in

Figure 4.2. It can be seen that the time to reach a statistically stationary state decreases with increasing Reynolds number. The trend is the same as for circular cylinder flow. The average drag coefficients are shown in Table 4.1. The drag coefficient decreases when Re increases from 60 to 100 and increases when Re increases from 100 to 150. The drag coefficients for square cylinder flow are higher than for circular cylinder flow at each Re. The bluff square cylinder compared to the circular cylinder would cause larger flow separation which results in higher drag. The drag coefficients from the literature are also shown. The average difference is 13.28% which is greater than that of circular cylinder flow. The differences could be accounted for by the blockage ratio. Since the frequency is sensitive to domain size, the difference could be due to domain sensitivity.
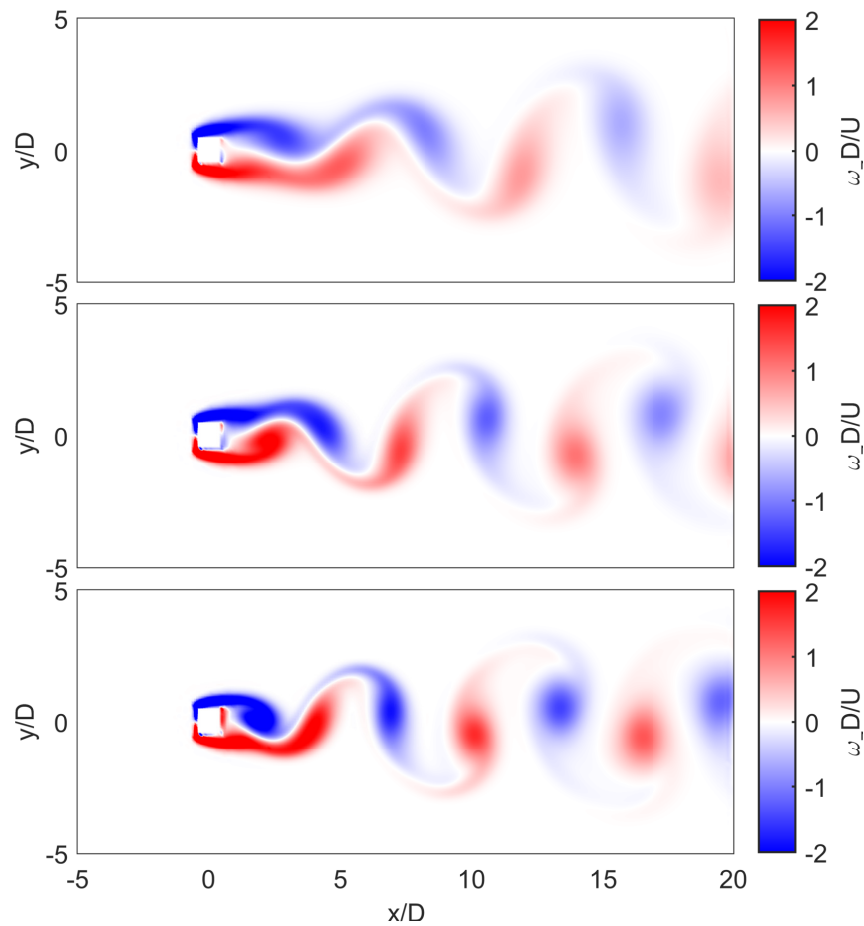
Figure 4.1. Visualization of vorticity of square cylinder flow at $Re = 60$(top), 100(middle), and 150(bottom).
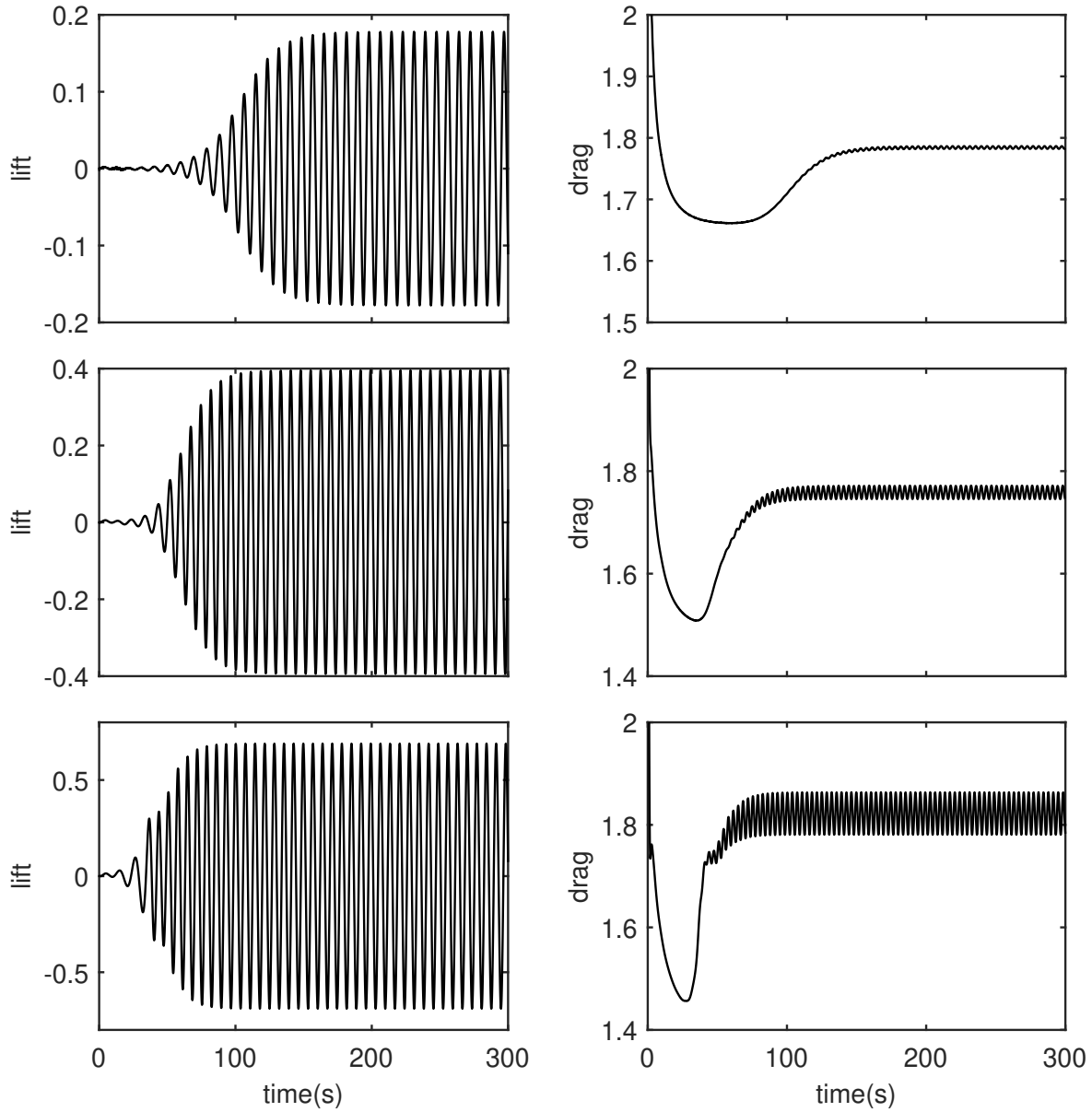
Figure 4.2. Evolution of lift and drag coefficients in time for flow over a square cylinder at *Re* of 60(top), 100(middle), and 150(bottom). The lift and drag coefficients in Table 4.1 are calculated as the time average of the instantaneous lift and drag coefficients in the statistically stationary stage.

**Table 4.1.** Drag Coefficients and Strouhal Numbers for Square Cylinder Flow

Source	Re	C_d	Relative Difference (%)	St	Relative Difference (%)	Method
This study	60	1.7658	—-	0.1172	—-	Numerical
This study	100	1.7517	—-	0.1367	—-	Numerical
Robichaux [20]		1.53	14.5	0.154	11.23	Numerical
Wang [30]		1.52	15.24	0.15	8.87	Numerical
Franke [8]		1.61	8.8	0.154	11.23	Numerical
Davis [6]		1.66	5.52	0.16	14.56	Experimental
Davis and Moore [5]		1.63	7.47	0.15	8.87	Numerical
Kelkar [12]		1.8	2.68	0.13	5.15	Numerical
Sohankar [26]		1.478	18.5	0.146	6.37	Numerical
This study	150	1.8201	—-	0.1465	—-	Numerical
Robichaux [20]		1.42	28.2	0.198	26	Numerical
Franke [8]		1.56	16.67	—-	—-	Numerical
Sohankar [26]		1.58	15.2	0.16	8.44	Numerical

4.1.2   SPOD Analysis

The spectra plots are shown in Figure 4.3. The gap between the largest and second largest eigenvalue is the largest at Re=60 and the smallest at Re=100. The Strouhal numbers are 0.1172, 0.1367, and 0.1465 for $Re = 60$, 100, and 150. The Strouhal number is higher at a larger Reynolds number, a similar trend as circular cylinder flow. The Strouhal numbers for square cylinder flow are in general lower than those of circular cylinder flow. The Strouhal numbers from this study and literature are shown in Table 4.1. The mean difference is 11.19% which is also larger than that of the circular cylinder. The St values are closer to the literature ones than the drag coefficients are. The same reason mentioned in the previous section can be the cause of the difference in St. The SPOD modes are shown in Figure 4.4. The patterns of the eigenmodes are similar to those from circular cylinder flow. The symmetric patterns at St and $3St$ and the anti-symmetric patterns at $2St$ persist. The magnitude of eigenmodes is similarly large near and away from the centerline at Re=60, but is larger near the centreline and smaller away, at Re=150.
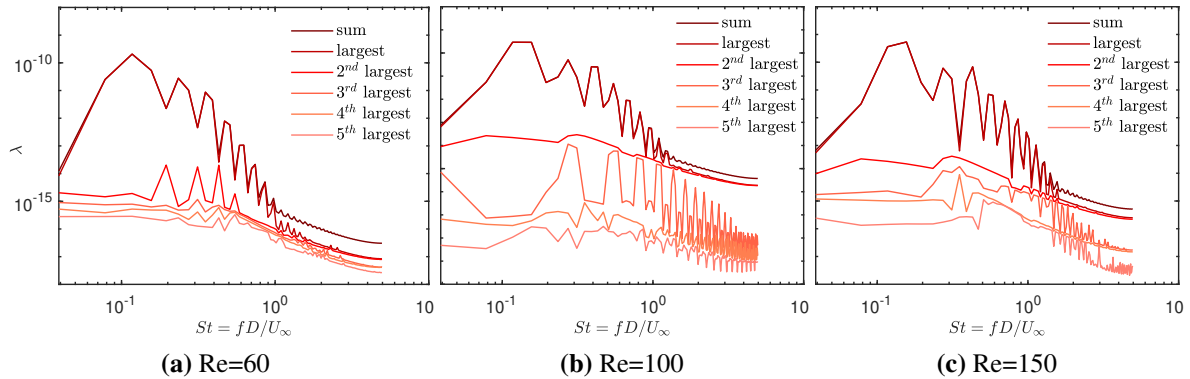
Figure 4.3. SPOD spectra for square cylinder flow at *Re* = 60(left), 100(middle), 150(right). The non-dimensional vortex shedding Strouhal numbers are 0.1172, 0.1367, and 0.1465.
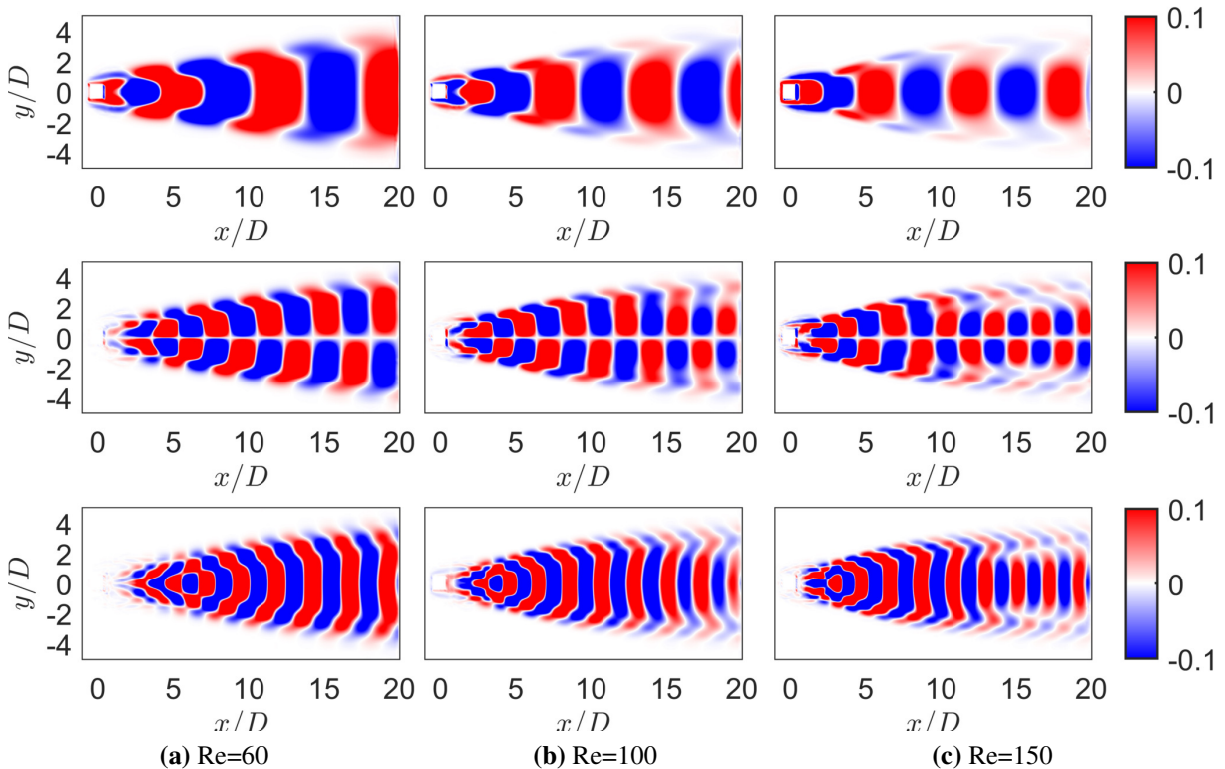
**Figure 4.4.** The leading SPOD modes at *St*(top), 2*St*(middle), and 3*St*(bottom) at *Re* = 60(left), 100(middle), and 150(right). To show the relative amplitude difference, the modes are normalized by the largest amplitude in the same plane.

This is due to the larger diffusivity at a lower Reynolds number.

4.2   Varying the Aspect Ratio of An Elliptical Cylinder

A circular cylinder is a specific case of an elliptical cylinder with an aspect ratio of 1. The aspect ratio (AR) is defined as the ratio of the diameter parallel to the incoming flow(a) to the diameter normal to the flow(b), a/b, as shown in Figure 4.5. Besides the special case of
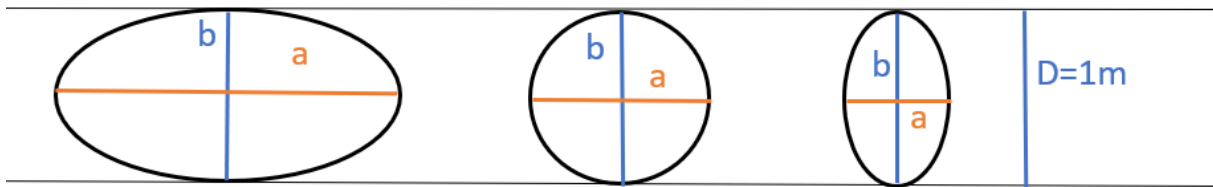

Figure 4.5. Example of elliptical cylinders with Aspect Ratio($AR = a/b$) of 2(left), 1(middle), and 0.5(right). $D = b = 1m$ is set as the characteristic length perpendicular to the freestream, which is a fixed constant in all simulations of elliptical cylinder wakes. The center of each object is placed at the origin in the simulation.

circular cylinders, elliptical cylinders with different aspect ratios at a fixed *Re* of 150 will also be analyzed. Aspect ratios of elliptical cylinders of 0.25, 0.5, 2, and 4 are studied. The length perpendicular to the direction of the freestream (*b*) is used as the characteristic body length scale. Simulation and SPOD analysis on the new cases are done with the same setting as before.

4.2.1   Flow Visualization

The vorticity is shown in Figure 4.6. The AR=1, AR=2, and AR=4 cases have the typical Karman vortex street feature. For the AR=0.5 and AR=0.25 cases, the vorticity in the far wake is different from other cases. Instead of the Karman vortex street where vortices shed alternately, the wake splits into two layers where vortices stay either above or below the centerline. The different vortex behavior will be analyzed in later section. The flow property for AR = 2 is similar to the one for AR=1 thus we will not discuss that case in the following sections.

The lift and drag coefficients are plotted with respect to time for each case. The AR
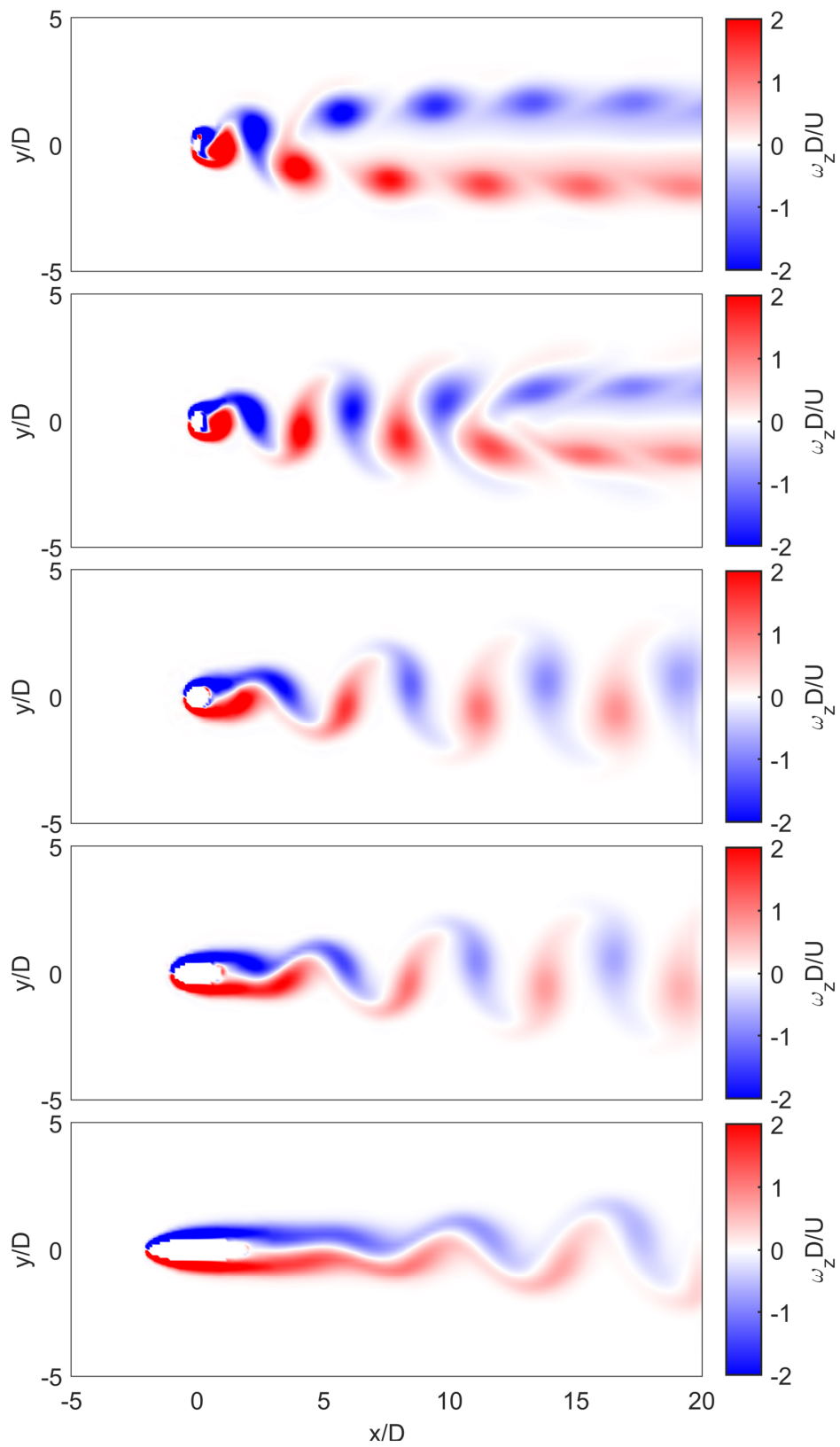
Figure 4.6. Visualization of vorticity at *Re*=150 with AR of 0.25, 0.5, 1, 2, 4 from top to bottom. The central cross-section facing the freestream of each obstacle is the same. Vorticity is normalized by convective units.

26

= 4 case takes a noticeably longer time to reach the statistically stationary state than all other cases. The averaged drag coefficients are shown in Table 4.2. The drag coefficient is higher at lower AR. This is because a bluff body has a larger drag coefficient compared to a streamlined body in general. The drag coefficients from the literature, shown in Table 4.2, are significantly lower than the result from this study. The average difference is around 16%. This is similar to square cylinder cases where all drag coefficients are larger than those from the literature. The large difference could also be due to domain sensitivity. The lower the frequency is, the more sensitive it is to the domain width, especially in 2D flows. Our numerical frequencies are consistently higher than theirs, suggesting that they are errors rather than uncertainty. This discrepancy motivated domain sensitivity study in the next chapter.

Table 4.2. Drag coefficients and Strouhal numbers for elliptical cylinder flow

Source	AR	C_d	Relative Difference (%)	St	Relative Difference (%)	Method
This study	0.25	2.3865	—-	0.1953	—-	Numerical
	0.5	2.0434	—-	0.1953	—-	Numerical
	1	1.3329	—-	0.1823	—-	Numerical
	4	0.9421	—-	0.1562	—-	Numerical
Thompson[27]	0.25	2.005	19.02	0.1650	18.36	Numerical
Shi [24]	0.25	2.068	15.40	0.1670	16.95	Numerical
Thompson[27]	0.5	1.779	14.86	0.1891	3.28	Numerical
Shi [24]	0.5	1.824	12.03	0.1910	2.25	Numerical

4.2.2   SPOD Eigenspectra

The spectra plots are shown in Figure 4.8. The peaks are at frequencies of 0.1953, 0.2009, 0.1823, and 0.1562 for AR of 0.25, 0.5, 1 and 4. The St is higher for smaller AR, i.e. bluffer body. However, the St for AR=0.25 and AR=0.5 are the same. This could be due to the behavior of vortices at far wake. The St numbers are compared to literature in Table 4.2. For both AR=0.25 and AR=0.5 cases, the resulting St is higher than the literature. The difference of 0.5AR case

27
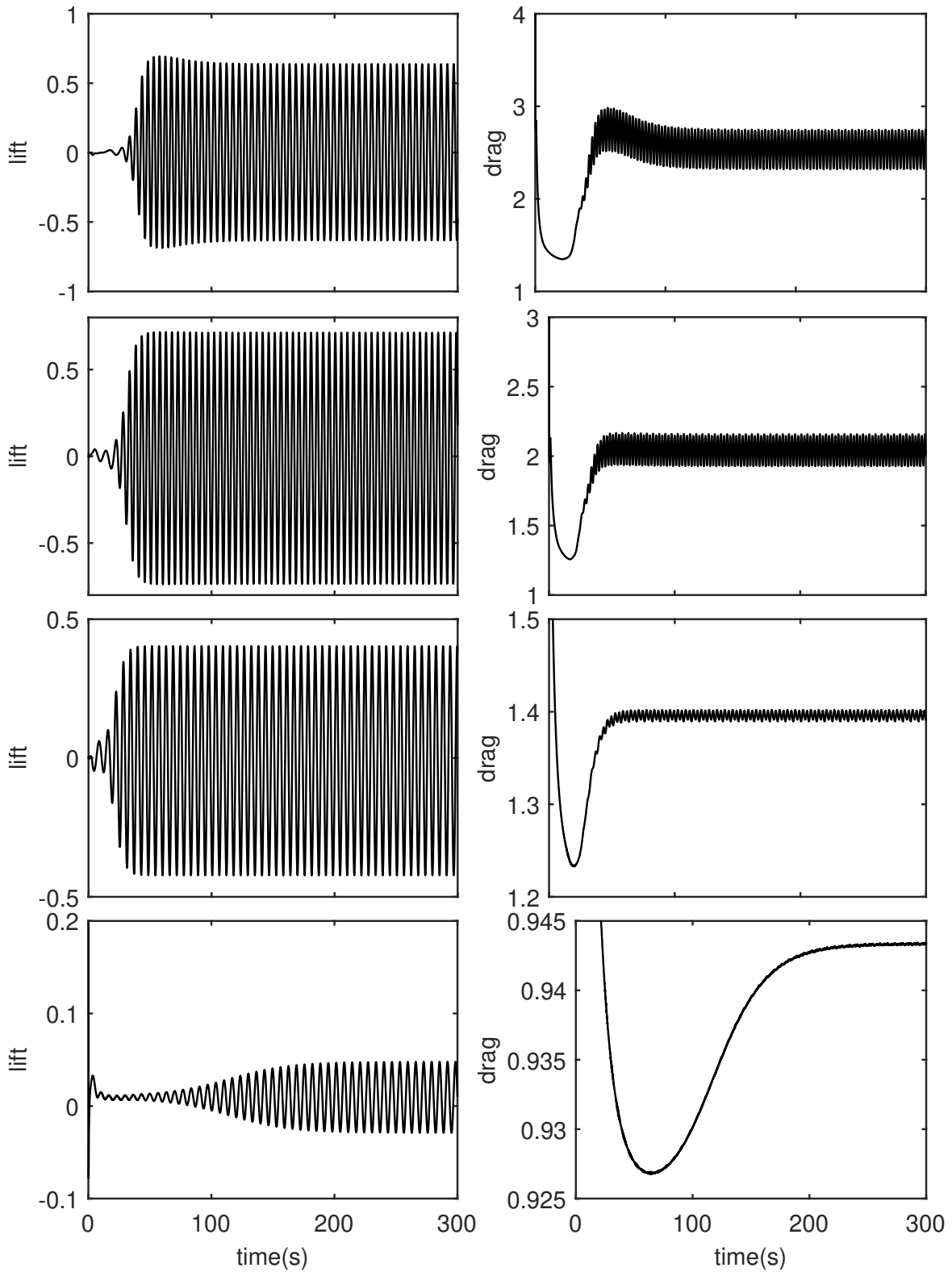
Figure 4.7. Evolution of lift and drag in time for flow over the elliptical cylinder with AR of 0.25, 0.5, 1, 4 from top to bottom at *Re*=150. The lift and drag coefficients in Table 4.2 are calculated as the time average of the instantaneous lift and drag coefficients in the statistically stationary stage.
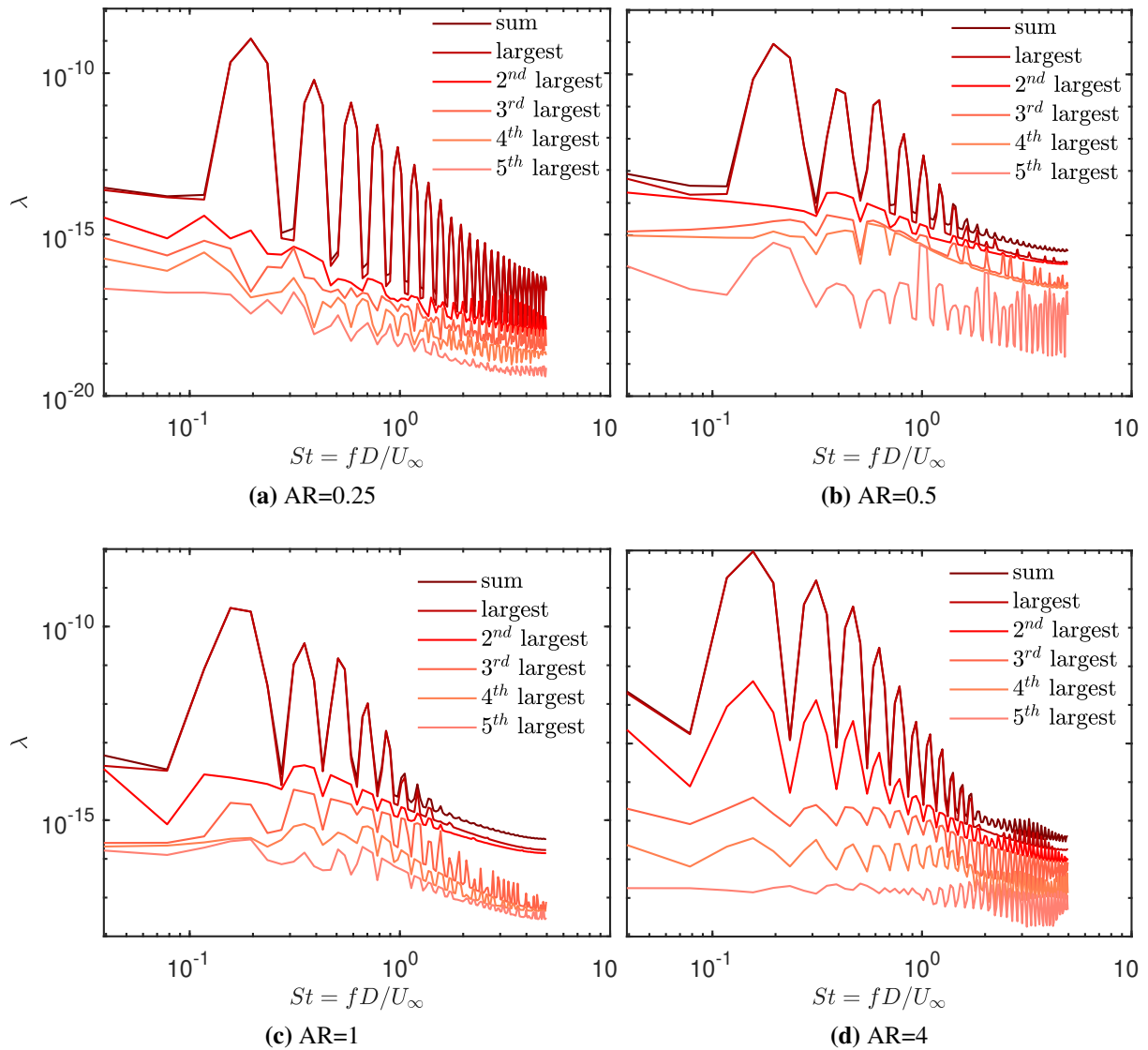
Figure 4.8. SPOD spectra plots for elliptical cylinder flow at *Re*=150 with AR of 0.25(top left), 0.5(top right), 1(bottom left) 4(bottom right). The non-dimensional shedding frequencies are 0.1953, 0.1953, 0.1823 and 0.1562. And subsequent peaks are the harmonics of the shedding frequencies.
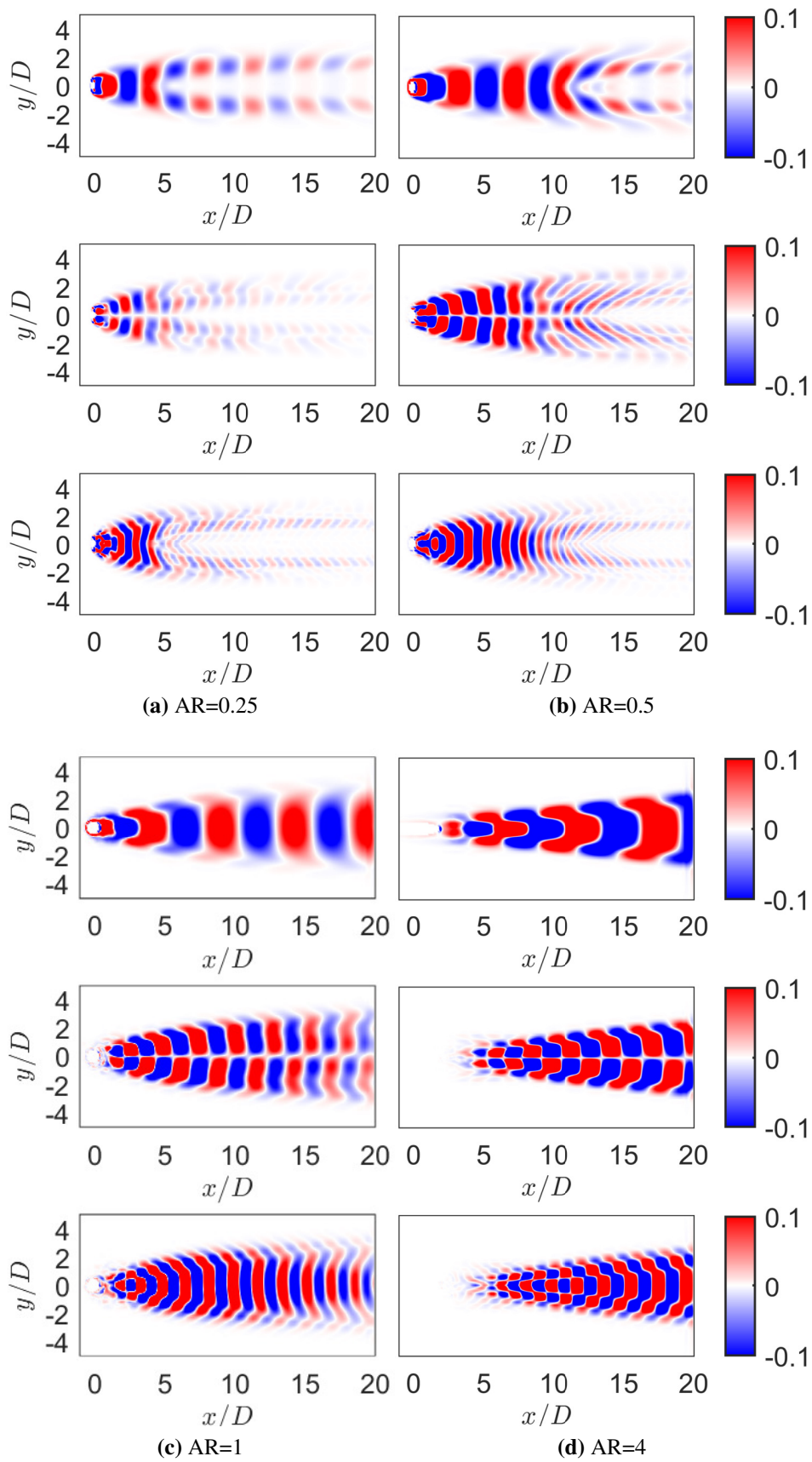
Figure 4.9. (a-d)For each subplot, the modes are associated with the frequencies at *St*(top), 2*St*(middle), and 3*St*(bottom) with AR=0.25, 0.5, 1, 4 respectively.

is around 3.3% but the difference of 0.25AR case is around 18.36%. The huge difference is believed to be caused by the sensitivity to domain size. The low-frequency modes are damped to give way to higher-frequency modes for 2D simulations of finite spanwise domains.

The simulation done by Thompson, Radi, Rao, Sheridan, et al.(2014) used [-50D,280D] in *x* and [-50D,50D] in *y* domain while our study used [-10D,20D] in *x* and [-10D,10D] in y. In the larger *x* domain considered by Thompson, the flow shows different behavior in the far wake. The behavior of vortices for AR=0.25 and AR = 0.5 cases is of interest farther downstream. Simulation done using a larger domain will be discussed in Section 4.3.

4.2.3 SPOD Eigenmodes

The modes are shown in Figure 4.9. The symmetric and anti-symmetric structures are observed in all elliptical cylinder cases as well. The AR = 4 case has similar structures as the circular cylinder case. The AR = 0.5 and AR = 0.25 cases show a split of modes from the centerline at the far wake, which corresponds to the vorticity plots. The modes for AR = 0.5 and AR = 0.25 cases before the split are similar to the modes from other cases. The location where the split of modes exists is close to the location where vortices start to split. The split appears closer to the cylinder body for AR = 0.25 case than AR = 0.5 case.

4.3 Sensitivity to Domain Length

In order to observe the behavior of flow in the far wake inspired by Thompson [27], we expand the domain to [-10D, 50D] in *x* direction and [-20D, 20D] in *y* direction. Simulation at *Re* = 150 for elliptical cylinders with AR of 0.25, 0.5, 1, and 4 will be discussed in this section.

4.3.1 Flow Properties

Vorticity plots from the simulations in the new longer and wider domain are shown in Figure 4.10. For the AR = 4 case, the vortices continue to have the Karman vortex feature. For AR = 1 case, the wake downstream has the two-layered feature that appeared for AR = 0.5, 0.25

cases in the shorter domain. For AR = 0.5 case, after the occurrence of the two-layered wake, the mean wake structure appears. For AR = 0.25 case, after the two-layered wake section, the wake starts to oscillate again forming a secondary vortex street.
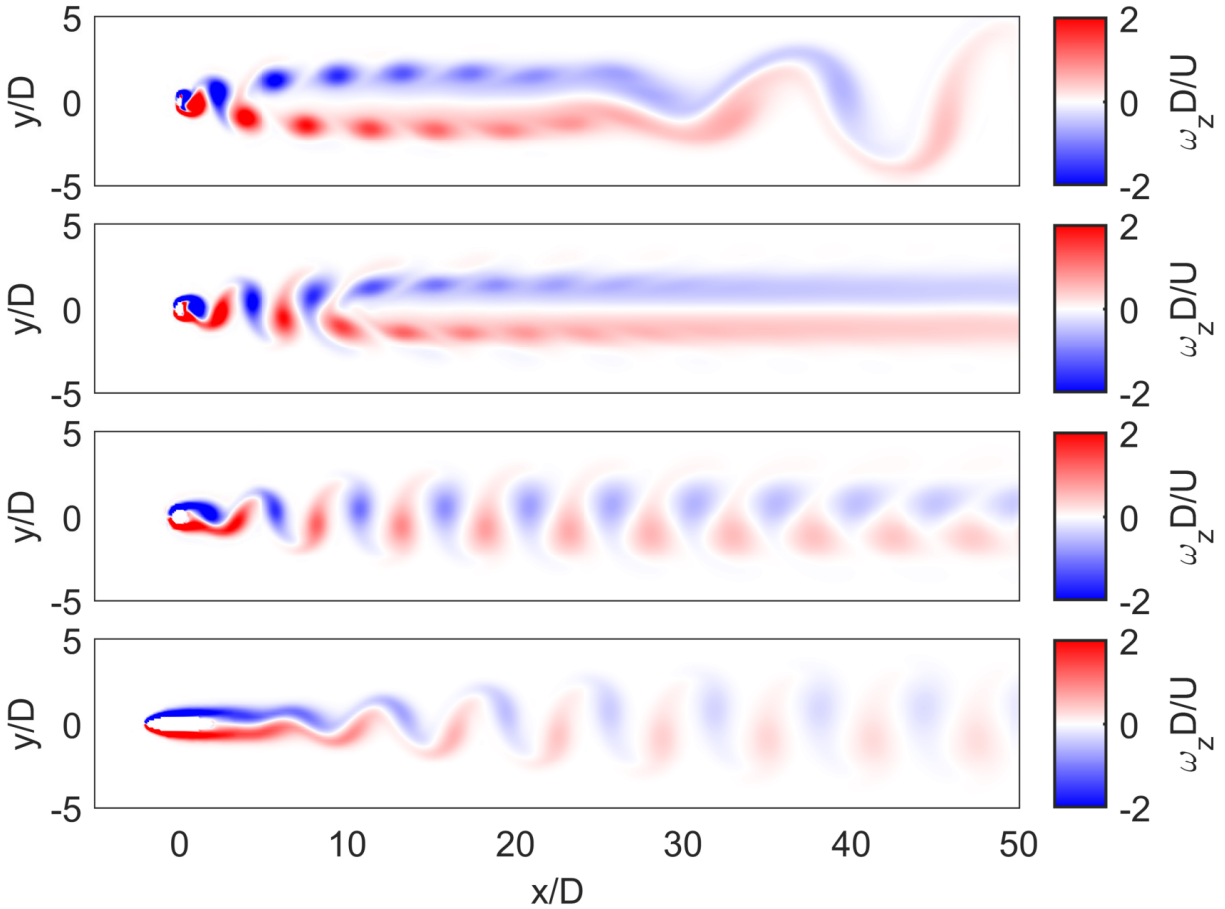
Figure 4.10. Visualization of vorticity plots at *Re*=150 with AR of 0.25, 0.5, 1, 4 from top to bottom in the larger domain. Vorticity is normalized by convective units. The secondary vortex can be seen on the top plane.

4.3.2   SPOD Analysis

The new spectra plots are shown in Figure 4.11. The Strouhal numbers are 0.1758, 0.1953, 0.1823, 0.1562 for AR of 0.25, 0.5, 1 and 4. The Strouhal number for 0.25AR is 9.98% lower in the larger domain than in the original domain. The new Strouhal number is close to the data from the literature and the difference reduces to 6.55%. For AR = 0.25 cases, there exists a secondary lower frequency (St_{sec}) of 0.0781. The lower frequency corresponds to the secondary

32

(a) AR=0.25

(b) AR=0.5

(c) AR=1

(d) AR=4
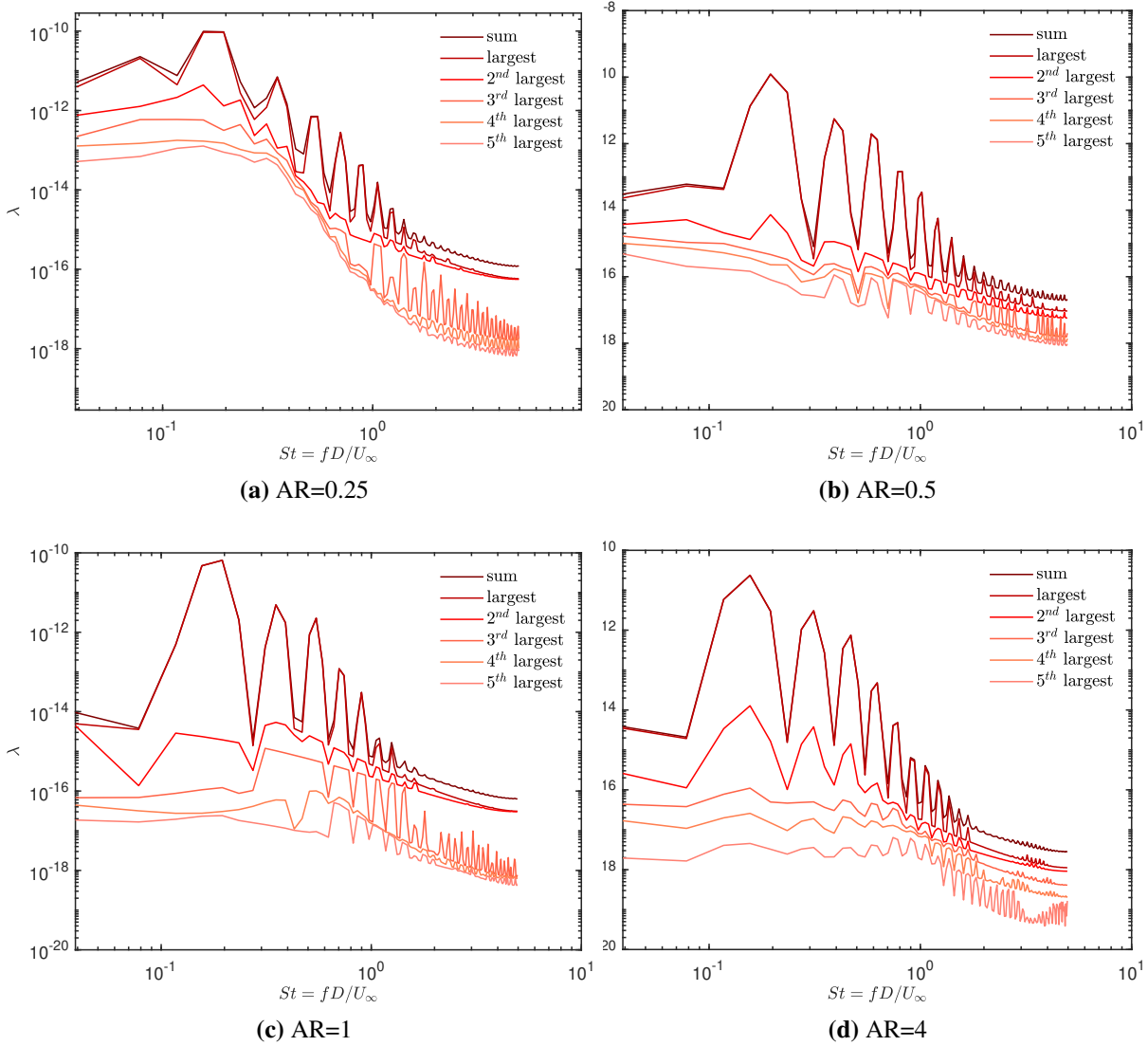
Figure 4.11. SPOD spectra plots for elliptical cylinder flow at *Re*=150 with AR of 0.25(top left), 0.5(top right), 1(bottom left) 4(bottom right) at the larger domain. The non-dimensional shedding frequencies are 0.1758, 0.1953, 0.1823 and 0.1562. And subsequent peaks are the harmonics of the shedding frequencies. The lower frequency peak for AR = 0.25 case is at 0.0781, which is St_sec defined in the text.

vortex street shown in the visualization. In Johnson's paper(2004), they found the secondary frequency to be 0.072. The difference is 8.47%. The difference of St and lower frequency is believed to be caused by the different domain sizes.
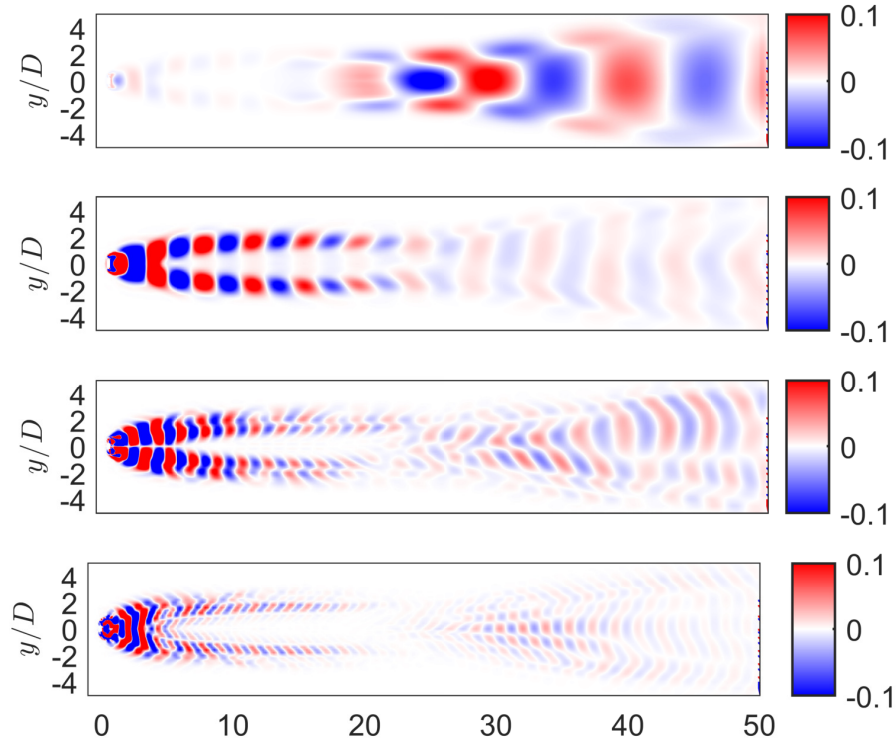

Figure 4.12. SPOD modes for AR=0.25 at Re=150 at St_{sec}, St, $2St$, $3St$ from top to bottom in the larger domain.

4.3.3   Secondary Vortex Street

The SPOD modes for Re=150, 0.5AR case at St_{sec} and Sts are plotted in Figure 4.12. The lower frequency of $St_{sec} = 0.0781$ has the most energy in the far wake where the secondary vortex street shows up. The mode for the secondary vortex street looks similar to the mode of a normal Karman vortex street. For the St, $2St$, and $3St$ cases, the near wake is more energetic, corresponding to the decay of the magnitude of Karman vortices downstream. The modes at far wake are neither symmetric nor anti-symmetric. The change of mode structures starts at about $23D$ which is approximately the location where the secondary vortex street showed up in the vorticity plot.

The secondary vortex street turns out not to be unique to the case of AR = 0.25. In Kumar and Mittal (2012), they found that for circular cylinder flow at Re = 150, there exists such a secondary vortex street as well in a longer domain. They believe the secondary vortex street is a result of the convective instability of the time-averaged wake.

The centerline transverse fluctuation energy ($< v'^2 >$) in the case where the secondary vortex street was observed is plotted. The $< v'^2 >$ for the original domain decreases downstream.
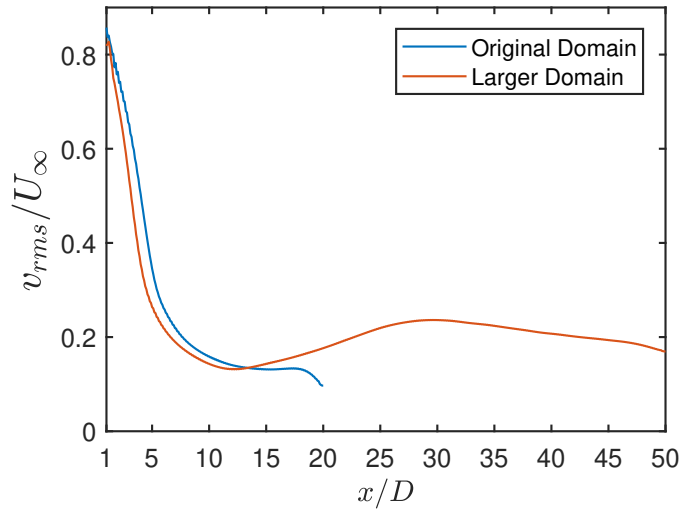
Figure 4.13. The centerline transverse fluctuation energy ($< V'^2 >$) plot for elliptical flow with AR = 0.25.

However, with the larger domain, there is an increase between about $12x/D$ to $28x/D$. The increase indicates the emergence of the secondary vortex street. The location where the increase emerges corresponds to the vorticity plot where the centerline starts to flap.

4.4   Comparison

The Strouhal numbers for circular, elliptical, and square cylinders are shown in Figure 4.14. *St* is higher at higher *Re*. Square cylinder flow has lower *St* than circular cylinder flow. For *Re*=150, AR=0.5 has the highest *St*. The *St* for AR=0.25 is lower than the circular cylinder but higher than the AR=4 case. The reason could be the existence of the low frequency. Square

cylinder flow has the lowest *St* among all. The square cylinder and elliptical cylinder cases have a greater difference between our *St* and literature ones than circular cylinder cases. This could be due to more bluff body and sharp corners.
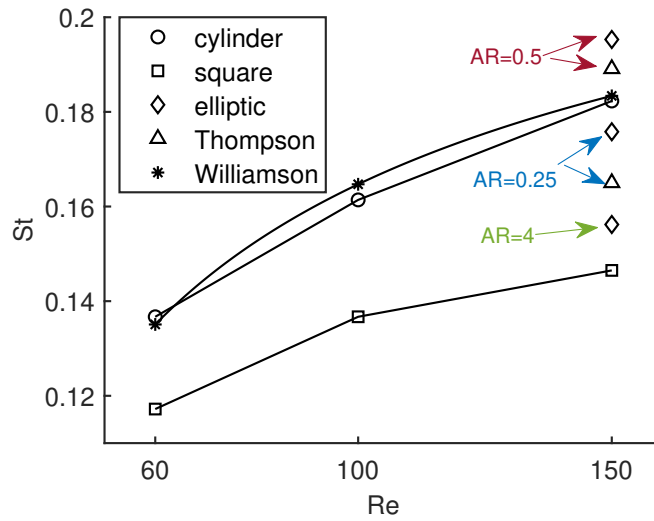
Figure 4.14. Comparison of *St* from cylinder, elliptical, square cylinder flow at *Re* = 60, 100, 150. Cylinder data is shown from Williamson [32] and elliptic cylinder data at AR = 0.5 and 0.25 are shown from Thompson et al. [27].

Chapter 5

Summary and Conclusions

In the present study, we simulate 2D flow over different shaped cylinders at different Reynolds numbers. We use SPOD to analyze the vorticity and find the Strouhal numbers and eigenmodes. The circular cylinder flow and square cylinder flow are simulated at Re of 60, 100, and 150. The elliptical cylinder flow is analyzed at $Re = 150$ and AR of 0.25, 0.5, and 4. At the considered Re values, the wake is known to be 2D, unsteady laminar without 3D turbulence. For the circular cylinder, the averaged drag coefficients and Strouhal numbers are close to the literature, which demonstrates the reasonable resolution of the present simulations. Differences with literature are somewhat larger for the square and elliptical cylinders and generally range between 5 to 15%. The large difference can be due to the lack of grid resolution at the square corners and high-curvature ends of the elliptical cylinders. The St for the square cylinder is systematically lower than in literature.

The spatiotemporal coherent structures are analyzed via SPOD, and the prominent modes are the vortex shedding modes. The vortex shedding Strouhal number increases as the Reynolds number increases. In terms of spatial structures, eigenmodes at St and $3St$ have symmetric structures about the centerline while the modes at $2St$ have anti-symmetric structures.

The square cylinder exhibits lower St relative to the circular cylinder (Figure 4.14) at each Re that was simulated. The drag is also larger than that of the circular cylinder. Similar to the cylinder, the Strouhal numbers for the square cylinder are larger at higher Re. The Strouhal

number for the elliptical cylinder increases from AR = 0.25 to AR = 0.5 and decreases from AR = 0.5 to AR = 4. The eigenmodes for square and elliptical cylinders show similar symmetric and anti-symmetric structures as circular cylinder flow.

For the elliptical cylinder cases, the simulations are redone with a larger domain constructed by increasing the downstream streamwise domain length from $20D$ to $50D$ and expanding the lateral boundaries from ± 10 to ± 20. The AR = 0.25 and 0.5 cases show a significant change downstream of $x = 20D$. The AR = 0.25 case exhibits a secondary low-frequency vortex street at the far wake, which is not found in the other cases within the domain of simulation. The corresponding frequency is found to be 0.0781. In the near and intermediate wake of the AR = 0.25 case, the vortex array takes the form of two rows of compact vortices that occupy opposite lateral half-planes ($y < 0$ and $y > 0$). Beyond $x \approx 25D$, the topology changes to a sinuous instability with each vortex extending across the entire lateral wake width. The AR = 0.5 case also exhibits a qualitative change from the near to the far wake. The near-wake vortices dissipate and the flow becomes laminar steady beyond $x = 30D$. The mode at the secondary frequency has similar structures as the mode of a normal Karman vortex street at the far wake but just with a different size.

In conclusion, the commercial software Ansys Fluent gives results for vortex shedding and the vortex wake structure in the 2D, laminar unsteady regime that are in reasonable quantitative agreement with previous literature. SPOD analysis sharpens the analysis of spatiotemporal coherence of the wake by proving leading eigenmodes at the dominant vortex shedding frequency and its harmonics. The effects of Reynolds number and of the body shape are well captured in the simulated range of $60 \leq Re \leq 150$.

Bibliography

[1]   D. Barkley. "Linear analysis of the cylinder wake mean flow". *Europhysics Letters* 75.5 (2006), p. 750. DOI: 10.1209/epl/i2006-10168-7. URL: https://dx.doi.org/10.1209/epl/i2006-10168-7.

[2]   Dwight Barkley and Ronald D. Henderson. "Three-dimensional Floquet stability analysis of the wake of a circular cylinder". *Journal of Fluid Mechanics* 322 (1996), pp. 215–241. DOI: 10.1017/S0022112096002777.

[3]   E Berger and R Wille. "Periodic Flow Phenomena". *Annual Review of Fluid Mechanics* 4.1 (1972), pp. 313–340. DOI: 10.1146/annurev.fl.04.010172.001525. eprint: https://doi.org/10.1146/annurev.fl.04.010172.001525. URL: https://doi.org/10.1146/annurev.fl.04.010172.001525.

[4]   M. Braza, Patrick Chassaing, and Ha H. "Numerical Study and Physical Analysis of the Pressure and Velocity Field in the Near Wake of a Circular Cylinder". *Journal of Fluid Mechanics* 165 (1986), pp. 79–130. DOI: 10.1017/S0022112086003014.

[5]   R. W. Davis and E. F. Moore. "A numerical study of vortex shedding from rectangles". *Journal of Fluid Mechanics* 116 (1982), pp. 475–506. DOI: 10.1017/S0022112082000561.

[6]   R. W. Davis, E. F. Moore, and L. P. Purtell. "A numerical-experimental study of confined flow around rectangular cylinders". *The Physics of Fluids* 27.1 (1984), pp. 46–59. ISSN: 0031-9171. DOI: 10.1063/1.864486. eprint: https://pubs.aip.org/aip/pfl/article-pdf/27/1/46/12743530/46_1_online.pdf. URL: https://doi.org/10.1063/1.864486.

[7]   Uwe Fey, Michael König, and Helmut Eckelmann. "A new Strouhal–Reynolds-number relationship for the circular cylinder in the range 47$<Re$<2×105". *Physics of Fluids* 10.7 (1998), pp. 1547–1549. ISSN: 1070-6631. DOI: 10.1063/1.869675. eprint: https://pubs.aip.org/aip/pof/article-pdf/10/7/1547/12487844/1547_1_online.pdf. URL: https://doi.org/10.1063/1.869675.

[8]   R. Franke, W. Rodi, and B. Schönung. "Numerical calculation of laminar vortex-shedding flow past cylinders". *Journal of Wind Engineering and Industrial Aerodynamics* 35 (1990), pp. 237–257. ISSN: 0167-6105. DOI: https://doi.org/10.1016/0167-6105(90)90219-3. URL: https://www.sciencedirect.com/science/article/pii/0167610590902193.

[9]   Carl A. Friehe. "Vortex shedding from cylinders at low Reynolds numbers". *Journal of Fluid Mechanics* 100.2 (1980), pp. 237–241. DOI: 10.1017/S0022112080001127.

[10]   Morteza Gharib and Philip Derango. "A liquid film (soap film) tunnel to study two-dimensional laminar and turbulent shear flows". *Physica D: Nonlinear Phenomena* 37.1 (1989), pp. 406–416. ISSN: 0167-2789. DOI: https://doi.org/10.1016/0167-2789(89)90145-0. URL: https://www.sciencedirect.com/science/article/pii/0167278989901450.

[11]   Shaun A. Johnson, Mark C. Thompson, and Kerry Hourigan. "Predicted low frequency structures in the wake of elliptical cylinders". *European Journal of Mechanics - B/Fluids* 23.1 (2004). Bluff Body Wakes and Vortex-Induced Vibrations, pp. 229–239. ISSN: 0997-7546. DOI: https://doi.org/10.1016/j.euromechflu.2003.05.006. URL: https://www.sciencedirect.com/science/article/pii/S0997754603001055.

[12]   Kanchan M. Kelkar and Suhas V. Patankar. "Numerical prediction of vortex shedding behind a square cylinder". *International Journal for Numerical Methods in Fluids* 14.3 (1992), pp. 327–341. DOI: https://doi.org/10.1002/fld.1650140306. eprint: https://onlinelibrary.wiley.com/doi/pdf/10.1002/fld.1650140306. URL: https://onlinelibrary.wiley.com/doi/abs/10.1002/fld.1650140306.

[13]   Bhaskar Kumar and Sanjay Mittal. "Effect of blockage on critical parameters for flow past a circular cylinder". *International Journal for Numerical Methods in Fluids* 50.8 (2006), pp. 987–1001. DOI: https://doi.org/10.1002/fld.1098. eprint: https://onlinelibrary.wiley.com/doi/pdf/10.1002/fld.1098. URL: https://onlinelibrary.wiley.com/doi/abs/10.1002/fld.1098.

[14]   Bhaskar Kumar and Sanjay Mittal. "On the origin of the secondary vortex street". *Journal of Fluid Mechanics* 711 (2012), pp. 641–666. DOI: 10.1017/jfm.2012.421.

[15]   J. S. Leontini, M. C. Thompson, and K. Hourigan. "A numerical study of global frequency selection in the time-mean wake of a circular cylinder". *Journal of Fluid Mechanics* 645 (2010), pp. 435–446. DOI: 10.1017/S0022112009993132.

[16]   C. Liu, X. Zheng, C. Liao, C. Sung, T. Huang, C. Liu, X. Zheng, C. Liao, C. Sung, and T. Huang. "Preconditioned multigrid methods for unsteady incompressible flows". In: *35th Aerospace Sciences Meeting and Exhibit*. 1998. DOI: 10.2514/6.1997-445. eprint: https://arc.aiaa.org/doi/pdf/10.2514/6.1997-445. URL: https://arc.aiaa.org/doi/abs/10.2514/6.1997-445.

[17]   Xia Ma and George Em Karniadakis. "A low-dimensional model for simulating three-dimensional cylinder flow". *Journal of Fluid Mechanics* 458 (2002), pp. 181–190. DOI: 10.1017/S0022112002007991.

[18]   Sanjay Mittal. "Global linear stability analysis of time-averaged flows". *International Journal for Numerical Methods in Fluids* 58.1 (2008), pp. 111–118. DOI: https://doi.org/10.1002/fld.1714. eprint: https://onlinelibrary.wiley.com/doi/pdf/10.1002/fld.1714. URL: https://onlinelibrary.wiley.com/doi/abs/10.1002/fld.1714.

[19]   C. Picard and J. Delville. "Pressure velocity coupling in a subsonic round jet". *International Journal of Heat and Fluid Flow* 21.3 (2000), pp. 359–364. ISSN: 0142-727X. DOI: https://doi.org/10.1016/S0142-727X(00)00021-7. URL: https://www.sciencedirect.com/science/article/pii/S0142727X00000217.

[20] J. Robichaux, S. Balachandar, and S. P. Vanka. "Three-dimensional Floquet instability of the wake of square cylinder". *Physics of Fluids* 11.3 (1999), pp. 560–578. ISSN: 1070-6631. DOI: 10.1063/1.869930. eprint: https://pubs.aip.org/aip/pof/article-pdf/11/3/560/12265374/560_1_online.pdf. URL: https://doi.org/10.1063/1.869930.

[21] Anatol Roshko. "On the development of turbulent wakes from vortex streets". In: 1953. URL: https://api.semanticscholar.org/CorpusID:15843746.

[22] Hermann Schlichting and Klaus Gersten. *Boundary-Layer Theory*. 2017. ISBN: 978-3-662-52917-1. DOI: 10.1007/978-3-662-52919-5.

[23] Oliver T. Schmidt and Tim Colonius. "Guide to Spectral Proper Orthogonal Decomposition". *AIAA Journal* 58.3 (2020), pp. 1023–1033. DOI: 10.2514/1.J058809. eprint: https://doi.org/10.2514/1.J058809. URL: https://doi.org/10.2514/1.J058809.

[24] Xiaoyu Shi, Mahbub Alam, and Honglei Bai. "Wakes of elliptical cylinders at low Reynolds number". *International Journal of Heat and Fluid Flow* 82 (2020), p. 108553. ISSN: 0142-727X. DOI: https://doi.org/10.1016/j.ijheatfluidflow.2020.108553. URL: https://www.sciencedirect.com/science/article/pii/S0142727X19306769.

[25] LAWRENCE SIROVICH. "TURBULENCE AND THE DYNAMICS OF COHERENT STRUCTURES PART I: COHERENT STRUCTURES". *Quarterly of Applied Mathematics* 45.3 (1987), pp. 561–571. ISSN: 0033569X, 15524485. URL: http://www.jstor.org/stable/43637457 (visited on 11/15/2023).

[26] A. Sohankar, C. Norberg, and L. Davidson. "Low-Reynolds-number flow around a square cylinder at incidence: study of blockage, onset of vortex shedding and outlet boundary condition". *International Journal for Numerical Methods in Fluids* 26.1 (1998), pp. 39–56. DOI: https://doi.org/10.1002/(SICI)1097-0363(19980115)26:1⟨39::AID-FLD623⟩3.0.CO;2-P. eprint: https://onlinelibrary.wiley.com/doi/pdf/10.1002/%28SICI%291097-0363%2819980115%2926%3A1%3C39%3A%3AAID-FLD623%3E3.0.CO%3B2-P. URL: https://onlinelibrary.wiley.com/doi/abs/10.1002/%28SICI%291097-0363%2819980115%2926%3A1%3C39%3A%3AAID-FLD623%3E3.0.CO%3B2-P.

[27] Mark C. Thompson, Alexander Radi, Anirudh Rao, John Sheridan, and Kerry Hourigan. "Low-Reynolds-number wakes of elliptical cylinders: from the circular cylinder to the normal flat plate". *Journal of Fluid Mechanics* 751 (2014), pp. 570–600. DOI: 10.1017/jfm.2014.314.

[28] Aaron Towne, Oliver T. Schmidt, and Tim Colonius. "Spectral proper orthogonal decomposition and its relationship to dynamic mode decomposition and resolvent analysis". *Journal of Fluid Mechanics* 847 (2018), pp. 821–867. DOI: 10.1017/jfm.2018.283.

[29] D. J. Tritton. "Experiments on the flow past a circular cylinder at low Reynolds numbers". *Journal of Fluid Mechanics* 6.4 (1959), pp. 547–567. DOI: 10.1017/S0022112059000829.

[30] Gang Wang. "Large Eddy Simulations of Bluff-Body Wakes on Parallel Computers". AAI9712474. PhD thesis. USA, 1996. ISBN: 0591199564.

[31] C.-Y. Wen and C.-Y. Lin. "Two-dimensional vortex shedding of a circular cylinder". *Physics of Fluids* 13.3 (2001), pp. 557–560. ISSN: 1070-6631. DOI: 10.1063/1.1338544. eprint: https://pubs.aip.org/aip/pof/article-pdf/13/3/557/12631911/557_1_online.pdf. URL: https://doi.org/10.1063/1.1338544.

[32] Charles H. K. Williamson and G. L. Brown. "A SERIES IN $1/\sqrt{Re}$ TO REPRESENT THE STROUHAL–REYNOLDS NUMBER RELATIONSHIP OF THE CYLINDER WAKE". *Journal of Fluids and Structures* 12 (1998), pp. 1073–1085. URL: https://api. semanticscholar.org/CorpusID:121752198.